Article

Explicit Spatiotemporal Simulation of Receptor-G Protein Coupling in Rod Cell Disk Membranes

Johannes Schöneberg,[1] Martin Heck,[2,*] Klaus Peter Hofmann,[2] and Frank Noé[1,*]

[1]Department of Mathematics, Computer Science and Bioinformatics, Freie Universität Berlin, Berlin, Germany; and [2]Institut für Medizinische Physik und Biophysik, Charité, Universitätsmedizin Berlin, Berlin, Germany

ABSTRACT   Dim-light vision is mediated by retinal rod cells. Rhodopsin (R), a G-protein-coupled receptor, switches to its active form (R*) in response to absorbing a single photon and activates multiple copies of the G-protein transducin (G) that trigger further downstream reactions of the phototransduction cascade. The classical assumption is that R and G are uniformly distributed and freely diffusing on disk membranes. Recent experimental findings have challenged this view by showing specific R architectures, including RG precomplexes, nonuniform R density, specific R arrangements, and immobile fractions of R. Here, we derive a physical model that describes the first steps of the photoactivation cascade in spatiotemporal detail and single-molecule resolution. The model was implemented in the ReaDDy software for particle-based reaction-diffusion simulations. Detailed kinetic in vitro experiments are used to parametrize the reaction rates and diffusion constants of R and G. Particle diffusion and G activation are then studied under different conditions of R-R interaction. It is found that the classical free-diffusion model is consistent with the available kinetic data. The existence of precomplexes between inactive R and G is only consistent with the data if these precomplexes are weak, with much larger dissociation rates than suggested elsewhere. Microarchitectures of R, such as dimer racks, would effectively immobilize R but have little impact on the diffusivity of G and on the overall amplification of the cascade at the level of the G protein.

INTRODUCTION

In retinal rod cells, absorption of a photon by the visual G-protein-coupled receptor rhodopsin (R) initiates a cascade of biochemical reactions that eventually generates an electrical signal. A first stage of signal transduction and amplification is provided by the receptor-catalyzed nucleotide exchange in the rod G protein, transducin (G). R and G are located in disk membranes that fill the rod outer segment. Although R and G display fundamental similarities to other receptors and heterotrimeric $G_{\alpha\beta\gamma}$ proteins (1), the single-quantum detective function of the rod cell requires that both proteins have specific properties, including a very low basal activity to ensure low noise and a rapid and efficient sequential activation of multiple copies of the G protein by single activated molecules of the receptor. In the dark, the catalytic activity of rhodopsin is efficiently blocked by the covalently bound inverse agonist 11-*cis*-retinal. Light-induced *cis/trans* retinal isomerization triggers conformational changes in the receptor protein that culminate in an equilibrium between inactive Meta I (M1) and active Meta II (R*) intermediates (2,3). The G holoprotein is peripherally bound to the disk membrane by weak hydrophobic and ionic interactions. After the exchange of GDP for GTP in the R*-$G_{\alpha\beta\gamma}$ complex, the G protein dissociates and active G_α-GTP (G*) binds to a cGMP phosphodi-

esterase in a noncatalytic, stoichiometric interaction. The active G*-phosphodiesterase complex rapidly hydrolyzes cGMP, leading to the closure of cGMP-dependent ion channels in the plasma membrane of the rod outer segment. Ca^{2+}-dependent feedback leads to a delayed recovery of the dark concentration of cGMP. At the receptor level, deactivating proteins, namely, a receptor kinase and arrestin, bind to R* to mediate its phosphorylation and to cap it against further interaction with G. Deactivation by arrestin takes 0.2–0.3 s, thereby enabling sufficient G-protein activation. The whole system forms a closed signal-transduction module that transforms the input-signal photon into a transient receptor current that provides the electrical signal for the synapse of the rod (4).

Mathematical descriptions of the photocurrent response of retinal rod cells by a system of ordinary differential equations (ODEs) date back to the early seventies (5). Once the visual cascade was understood as a G-protein-coupled system, known partial steps were increasingly incorporated into schemes of differential equations describing signal transduction (6), eventually including downstream reactions (7,8) and leading to a full simulation of the electrical response.

In the dim-light working range of the rod, each disk membrane receives only one or a few photon hits, triggering the whole cascade. To study these single-photon responses, the stochastic spatiotemporal nature of the system had to be incorporated into the simulations. The

well-mixed assumption of ODE methods (i.e., ODEs have no concept of location, such as the position of the single activated rhodopsin) rendered these approaches not useful for our application. As a result, grid-based spatiotemporal chemical master equations (ST-CMEs) were used (9,10), allowing for discrete particle numbers rather than concentrations and a higher spatial resolution of the disk membrane. However, this method relies on the well-mixed assumption being true for small subspaces (i.e., lattice boxes), in which the system is discretized. In a different approach, partial differential equations (PDEs) were used on the photoactivation cascade to achieve the same goal of a higher spatial resolution (11–13). The PDE approach is also useful for deriving general theoretical results, such as first passage times in specific geometries (14–17). However, PDEs use concentrations of molecules and are therefore impractical when small particle numbers are important.

Recent experimental findings oppose the scenario of a well-mixed, free-diffusion, uniformly distributed disk membrane by reporting large rhodopsin clusters (18), immobile fractions of R (19), and special paracrystalline rhodopsin structures called racks of dimers (20).

The specific inhomogeneous architecture of these structures on all levels of detail together with the importance of individual molecules (a single R* triggers the cascade) goes beyond the limits of ST-CME and PDE methods. Individual molecules, arranged in their specific architectures, have been used in a Monte Carlo simulation to characterize the influence of such structures on the diffusion properties on the disk membrane (21). That study revealed a high impact of these structures on the diffusion but did not investigate their impact on reactions.

Such methods, which also treat reactions, are usually referred to as particle-based reaction-diffusion simulations (PBRD). Here, every molecule is represented individually in continuous space and time and its diffusion and reaction dynamics is simulated on a microscopic level. Individual molecules can be modeled as freely diffusing, as immobile obstacles, or in some trap potential. At the same time, reactions between particles can occur only upon physical encounter of reactive particles. In this way, complex interactions between particle mobility and reaction rates, such as inhibition of reactions due to spatial occlusion, can be investigated.

Covering all scenarios of rhodopsin architecture on a disk membrane requires single-particle resolution, particle diffusion, a simulation geometry, particle-particle interaction potentials, and reactions between particles. Other available tools (22–35) covered some but not all of these requirements. For this reason, the new PBRD package ReaDDy was developed (36). Using ReaDDy, we are able to test the effect of different supramolecular arrangements of R on molecule diffusivity and outcome of signal transduction at the same time.

We chose three representative cases to compare, namely, 1), the classic case, in which all particle species diffuse freely and are uniformly distributed; 2), the precomplex case, which is the same as case 1 but with an additional precomplex interaction between the inactive receptor and G (37); and 3), the rack case, where G diffuses freely and is uniformly distributed, but a large fraction of R is arranged in racks of dimers (20) and thereby rendered immobile (19).

For our model, a to our knowledge new set of kinetic rates of the G activation step was derived based on near-infrared light-scattering experiments using native disk membranes, as in a previous study (38). These rates give new insight into G-protein activation kinetics, revealing that the conformational changes leading from a receptor-G-protein encounter complex to an active complex and the GDP release are most probably the rate-limiting steps.

In using this set of kinetic rates in the particle-based simulation and combining it with the experimentally known kinetics of G-protein activation (38), we can assess the consistency of different R-architectures with experimental kinetics and give parameter ranges in which this consistency is provided.

The salient result of our study is that the supramolecular architecture has a surprisingly modest impact on the overall amplification of the cascade at the level of the G protein. It turns out that the diffusivity of the G-protein can override the influence of receptor architecture. An important exception is the case of precomplexes between R and G, which are only possible if they are formed very transiently. Considering the uniformity of the simulated signals, signal variability is moderate if there is only one fraction of receptor mobility present. Signal variability is increased by different fractions, i.e., mobile and immobile fractions of R, occurring at the same time (19).

Our derived model, at present containing the first steps of the photoactivation cascade including diffusion, crowding, molecular architecture, and detailed kinetics, can now serve as a building block for larger-scale physical simulations, e.g., of the entire signal cascade in a rod cell.
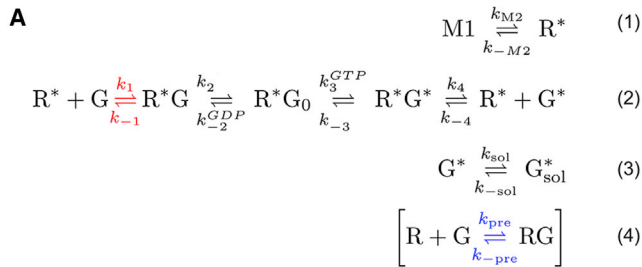
MATERIALS AND METHODS

Kinetic parameter derivation and ODE modeling

Based on the reaction scheme in Fig. 1 (Eqs. 1–4) and the scenario (with or without precomplexes), the kinetic reaction rates are estimated from enzymatic parameters obtained in a previous study (38). These experiments were conducted at 22°C with purified disk membranes. Rhodopsin concentrations were $[R] = 25,000 \ \mu m^{-2}$ and $[R^*] = 5.7 \ \mu m^{-2}$. G-protein activation ligand concentration was set to yield maximal G^* production rates: $[GDP]^0 = 0 \ \mu m^{-2}$ and $[GTP]^0 = 3000 \ \mu m^{-2}$.

Reaction rates were then determined by fitting the ODE model (Fig. 1 A) to experimental traces of G^*_{sol} production over time (Fig. 2 A). To verify the results, another series of dissociation signals measured in the presence of 200 μM GTP (0 μM GDP, data taken from (38)) were simulated with both sets of rate constants. As seen in Fig. 2 B, the resulting traces are in

ODE Model

A

$$M1 \underset{k_{-M2}}{\overset{k_{M2}}{\rightleftharpoons}} R^*$$ (1)

$$R^* + G \underset{k_{-1}}{\overset{k_1}{\rightleftharpoons}} R^*G \underset{k_{-2}^{GDP}}{\overset{k_2}{\rightleftharpoons}} R^*G_0 \underset{k_{-3}}{\overset{k_3^{GTP}}{\rightleftharpoons}} R^*G^* \underset{k_{-4}}{\overset{k_4}{\rightleftharpoons}} R^* + G^*$$ (2)

$$G^* \underset{k_{-sol}}{\overset{k_{sol}}{\rightleftharpoons}} G_{sol}^*$$ (3)

$$\left[R + G \underset{k_{-pre}}{\overset{k_{pre}}{\rightleftharpoons}} RG \right]$$ (4)

ReaDDy Model

B

$$R^* + G \underset{k_{-enc}^{R^*G}}{\overset{k_{enc}^{R^*G}}{\rightleftharpoons}} R^* \cdot G \underset{k_{-1}}{\overset{k_1^{micro}}{\rightleftharpoons}} R^*G$$ (2.2)

$$\left[R + G \underset{k_{-enc}^{RG}}{\overset{k_{enc}^{RG}}{\rightleftharpoons}} R \cdot G \underset{k_{-pre}}{\overset{k_{pre}^{micro}}{\rightleftharpoons}} RG \right]$$ (4.2)
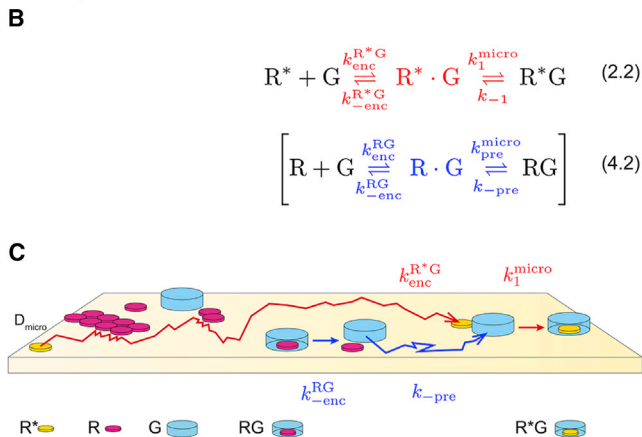
C

FIGURE 1   Reaction kinetics at two levels of modeling detail. (*A*) The first steps of the photoactivation cascade consist of the following activation reactions: M1/R* equilibrium (*1*); G-activation reactions, comprising formation of R*G complex, subsequent nucleotide exchange in G, and R*G*-complex dissociation (*2*); and dissociation of G* from the membrane (*3*). A nonproductive RG-complex formation (*4*) is added for the precomplex case. These reactions are used for the ODE model of the cascade. (*B*) Using particle-based reaction-diffusion (ReaDDy), bimolecular association reactions have to be split into the explicitly simulated diffusional encounter and the first-order transition from encounter complex to stable complex. This affects the R*G- and RG complex formation in (2.2) and (4.2) (*red* and *blu*e). (*C*) Graphical representation of the microscopic diffusion and reaction components, illustrating space exclusions, molecular shape, and crowding. To see this figure in color, go online.

good agreement with the experimental data (see Table 1 for the derived reaction rates and the Supporting Material for the details of rate derivation).

ReaDDy Model

The detailed spatiotemporal model was set up and simulated with the particle-based reaction-diffusion simulation software ReaDDy, version 1.1 (36). All molecules are modeled as spherical particles. These particles collide with each other if they get closer than the sum of their collision radii (r_c). These radii come in two types, $r_{c,mb}$, for membrane internal collisions, and $r_{c,sol}$, for the collisions of soluble parts of the molecules. A collision results in particle-particle repulsion, governed by a harmonic potential. If particles collide, such that the distance between them is smaller than the sum of their reaction radii (r_r), a reaction can be triggered. All radii are taken from crystal structures (39–42) (see Fig. 3 *A*). Due to the properties of the reference experiment (38), particle diffusion is confined to a spherical surface by applying a harmonic potential along the surface normal. The surface size (radius, $r = 120$ nm, and surface area, $A = 0.18$ μm^2) was chosen such that it would host on average 1 R*, 4499 R, and 450 G (see Fig. 3 *B*). The Brownian dynamics are integrated with a time step of $\Delta t = 20$ ns. Typi-
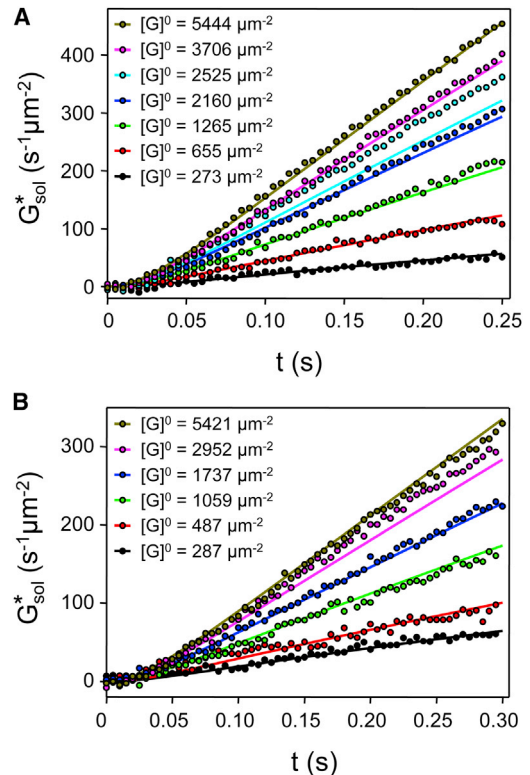
A

B

FIGURE 2   ODE fit and modeling. (*A*) ODE fits (*solid lines*) to representative dissociation signals (*circles*; measuring conditions and rate constants as in Tables 1, S1, and S2). (*B*) ODE modeling (*solid lines*) of representative dissociation signals (200 μM GTP, 0 μM GDP; values taken from Heck and Hofmann (38)), with rate constants as in Table 1. Note that the two sets of rate constants (sets A and B in Table S4) yield essentially identical traces. To see this figure in color, go online.

cally, the total simulation time is 200 ms, corresponding to 10^7 time steps; on a standard CPU (Intel Xeon E5345@2.33 GHz), this would take ~400 h. See the Supporting Material for a more detailed description of the ReaDDy model.

Microscopic modeling of diffusion and crowding

The simulation resolves all major disc membrane proteins explicitly and therefore, the diffusion constants used are those for a protein diffusing in a pure lipid membrane, D_0. Collisions between particles lead to crowding effects: Depending on particle density, mobility, and size (43–46), either normal diffusion but with a decreased diffusion constant, D, or anomalous diffusion with a time-dependent diffusion constant, $D(t)$, is observed on long timescales (47,48). Published values for rhodopsin and G protein correspond to such observed diffusion constants (19,49–54). D_0 is first parametrized in the free-diffusion case by sampling and theoretical calculations (see Fig. S3 in the Supporting Material). The effect of rhodopsin architecture is investigated by comparing D_0 and D.

Microscopic reaction modeling

In mass-action kinetics, bimolecular association rates, k_{on}^{macro}, incorporate both encounter complex formation due to diffusion (with rate k_{enc}) and actual complex formation (with rate k^{micro}). Since the diffusion is simulated explicitly in the ReaDDy simulation, k^{micro} has to be derived from k_{on}^{macro}. This is necessary for R*G- and RG-complex formation reactions, resulting in Eqs. 2.2 and 4.2 in Fig. 1. (The other two bimolecular reactions involve the small, cytosolic molecules GDP and GTP that diffuse orders of

TABLE 1 Experimental parameters and derived reaction rates

Parameter	Value	Description
T [a]	22°C	Temperature of the experiment
$[R]$ [a]	25,000 μm^{-2}	Rhodopsin density on disk vesicles
$[R^*]$, $[M1]$ [a,c]	5.7 μm^{-2}	Activated Rhodopsin density on disk vesicles
$[G]_1^{0a,e}$	273 μm^{-2}	Initial G density in first experiment
$[G]_2^{0a,e}$	1265 μm^{-2}	Initial G density in second experiment
$[G]_3^{0a,e}$	2525 μm^{-2}	Initial G density in third experiment
$[G]_4^{0a,e}$	5444 μm^{-2}	Initial G density in fourth experiment
$[GDP]^{0a}$	0 μm^{-2}	Initial GDP concentration in experiment
$[GTP]^{0a}$	3000 μm^{-2}	Initial GTP concentration in experiment
k_{M2} [b]	35.4 s^{-1}	Rate of M1 to R^* conversion of rhodopsin
k_{-M2} [b]	14.4 s^{-1}	Rate of R^*-to-M1 conversion of rhodopsin
k_1 [b]	0.36 $\mu m^2\ s^{-1}$	Rate of R^*G-complex formation
k_1^{micro} [d]	5000 s^{-1}	Microscopic rate of R^*G-complex formation
k_{-1} [b]	200 s^{-1}	Rate of R^*G-complex dissociation
k_2 [b]	600 s^{-1}	Rate of GDP release from R^*G complex
$k_{-2}^{GDP} = k_{-2}$ [GDP] [b]	2.2 $s^{-1}\mu M^{-1}$ [GDP]	Rate of GDP uptake by R^*G complex
$k_3^{GTP} = k_3$ [GTP] [b]	2.6 $s^{-1}\mu M^{-1}$ [GTP]	Rate of GTP uptake by R^*G complex
k_{-3} [b]	600 s^{-1}	Rate of GTP release by R^*G^* complex
k_4 [b]	60,000 s^{-1}	Rate of R^*G^* complex dissociation
k_{-4} [b]	0 s^{-1}	Rate of R^*G^* complex formation
k_{sol} [b]	10,000 s^{-1}	Rate of G^* membrane dissociation
k_{-sol} [b]	0 s^{-1}	Rate of G^* membrane binding
k_{pre}	1.67 $\mu m^2 s^{-1}$	Rate of RG-complex formation
k_{pre}^{micro} [d]	10^8 s^{-1}	Microscopic rate of R^*G-complex formation
k_{-pre}	11,200 s^{-1}	Rate of RG-complex formation

[a]Experimental conditions in (38).

[b]Rates were obtained via an ODE fitting procedure of experimental data (see methods and SI for details).

[c]ODE simulations start with $[M1] = 5.7\ \mu m^{-2}$, ReaDDy simulations start with $[R^*] = 5.7\ \mu m^{-2}$.

[d]Rate required for ReaDDy simulations only. Rate applies for the complexation reaction, once the particles are closer than their reaction radii.

[e]Concentrations used for both ReaDDy and ODE simulations. The ODE fit contained three additional experiments (see Table S2).

magnitude faster than do membrane-bound proteins and are therefore considered unimolecular on our timescales). See the Supporting Material for derivation of the microscopic reaction rates and Table 2 for the resulting parameters.

RESULTS AND DISCUSSION

Free-diffusion model

We first derive a model assuming that both R and G are uniformly distributed and freely diffusing. This is the simplest assumption for the experimental preparation described in Heck and Hofmann (38), which used R and G on purified membranes.

First, the diffusion constants of R and G are parametrized. As shown in the work of Saxton (43), no percolation threshold exists if obstacles and tracers (both being rhodopsin in this case) diffuse at the same rate. In such cases, the mean-squared displacement of particles, $\langle r^2 \rangle$, will start as $\langle r^2 \rangle \propto D_0$, will show anomalous diffusion for a short period of time, and will finally display normal diffu-

A R-type   G-type   RG-type

side view

collision radii

$r_{c,R,mb}$ $r_{c,G,mb}$ $r_{c,G,top}$ $r_{c,RG,mb}$ $r_{c,RG,top}$

top view

B
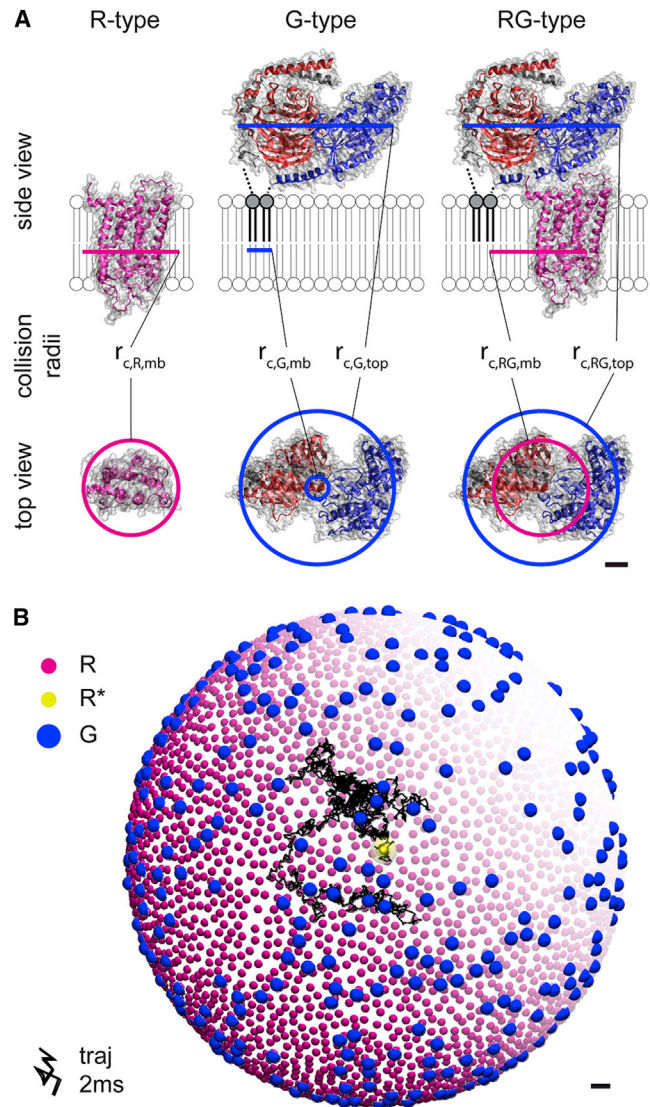
- ● R
- ● R*
- ● G

traj 2ms

FIGURE 3 ReaDDy model. (A) Collision radii of R-type, G-type, and RG-type particles were chosen based on crystal structures (R and R*, bovine 1U19 and 3PQR (40); G, bovine 1GOT (41); RG, 3SN6 (42)). Due to the different molecular shapes within and on the surface of the membrane, there are two types of collision radii: $r_{c,mb}$ for collisions within the membrane and $r_{c,sol}$ for collisions on the membrane surface (see Table 2 for radius parameters). (B) Disk-vesicle geometry with 4499 R (*purple*), 450 G (*blue*), and 1 R* (*yellow*) on a 0.18 μm^2 surface. The diffusion trajectory (*black line*; and see *inset*) of R* is drawn for 2 ms. To see this figure in color, go online.

sion with $\langle r^2 \rangle \propto D$ (43,44,48,56–59) (see Klafter and Sokolov (60) for an introduction to anomalous diffusion). In our case, we operate at an occupied area fraction of $c = 0.35$, given a rhodopsin density of 25,000 μm^{-2}. For this scenario, a crowding factor $D^*_{free} = D/D_0 = 0.5$ was calculated (43,61). Our model reproduces these calculations, resulting in the diffusion parameters presented in Table 2.

Reactions in the model include the Meta1-R* equilibrium of light-activated receptor (Eq. 1), G activation reactions

TABLE 2 Parameters of the ReaDDy model.

Parameter	Value	Description
$r_{vesicle}$	120 nm	Radius of the simulated vesicle
$A_{vesicle}$	0.18 μm^2	Surface area of the simulated vesicle
n_R[a,b]	4499	Number of rhodopsin particles on a vesicle
n_{R^*}[a,b]	1	Number of activated rhodopsins on a vesicle
$n_{G,1}$[a]	49	Initial number of Gs for first experiment simulation
$n_{G,2}$[a]	228	Initial number of Gs for second experiment simulation
$n_{G,3}$[a,b]	454	Initial number of Gs for third experiment simulation
$n_{G,4}$[a]	980	Initial number of Gs for fourth experiment simulation
$r_{c,R,mb}$[c]	2.1 nm	Collision radius of R-type particles within the membrane
$r_{r,R}$[c]	2.1 nm	Reaction radius of R-type particles
$r_{c,G,mb}$[d]	0.6 nm	Collision radius of G-type particles within the membrane
$r_{c,G,sol}$[d]	3.4 nm	Collision radius of G-type particles on top of the membrane
$r_{r,G}$[d]	3.0 nm	Reaction radius of G-type particles
$r_{c,RG,mb}$	2.1 nm	Collision radius of RG-type particles within the membrane
$r_{c,RG,sol}$	3.4 nm	Collision radius of RG-type particles on top of the membrane
k_{pot}[e]	10kJ/mol/nm^2	Force constant of the repulsive particle-particle potential, Eq S8.
Δt	20 ns	Integration timestep
D_0^R[f]	1.4 μm^2/s	Diffusion constant of R in free lipid.
D_0^G[f]	2.0 μm^2/s	Diffusion constant of G in free lipid.
D_{free}^*[f]	0.5	Crowding factor in free diffusion at density [R].
D_{free}^R[f]	0.7 μm^2/s	Apparent diffusion constant of R in the free scenario.
D_{free}^G[f]	1.2 μm^2/s	Apparent diffusion constant of G in the free scenario
D_{racks}^*[f]	0.26	Crowding factor in racks model at density [R].
D_{racks}^R[f]	0.4 μm^2/s	Apparent diffusion constant of R in the racks scenario.
D_{racks}^G[f]	0.8 μm^2/s	Apparent diffusion constant of G in the racks scenario

[a]Experimental conditions (38).
[b]Conditions referred to as native.
[c]Based on crystal structure 2I36 (55), see SI for detailed derivation.
[d]Based on crystal structure 1GOT, see SI for detailed derivation.
[e]See Supporting Information and Ref (36). for potential parametrization.
[f]Diffusion constants are based on values in (49), calculations in this work and (43,45), see SI for details.

(Eq. 2) and G* membrane dissociation (Eq. 3). In this model, no precomplex reaction is included (Eq. 4). To get a comprehensive set of reaction rates, a set of experimental G* traces of different G concentrations (Table S2) was fitted simultaneously to an ODE model of the reaction scheme (Fig. 2). Two sets of reaction rates were obtained, and both fit the data (Table S4). The two sets are similar as to the rates of the initial R*G complex formation and dissociation (k_1, k_{-1}) and the final G* membrane dissociation (k_{sol}). Once the R*G complex is formed, the rate-limiting step in G* production remains ambiguous. Placing the kinetic barrier on

GDP release or the final R*G*-complex dissociation, both fit the experiments equally well (compare rate sets A and B in Table S4). It is widely accepted that GDP release is generally rate-limiting in G-protein-coupled receptor systems for nucleotide exchange reactions (see review by Johnston and Siderovsky (62)). We therefore select rate set A and use it for all further investigations and microscopic simulations.

The association of G and R* (by k_1) is the only bimolecular reaction in our model that describes protein-protein interactions. Having parametrized all other reaction rates and model parameters, we can perform simulations with different values of k_1^{micro}, measure the resulting G_{sol}^* production, and choose the k_1^{micro} value that reproduces the experimental G_{sol}^* production rate (see the Supporting Material, especially Fig. S6, for the k_{micro} sampling setup). We observe that $k_1^{micro} = 5000$ s^{-1} matches experimental observations of 285 G_{sol}^*/R*/s (for a setup of [G] = 2525 μm^{-2}), leading to a reaction probability of 10^{-4} upon collision, given our chosen time discretization (see Eq. S12). The sampling reveals that the reaction does not operate at its diffusion limit, which is reached for $k_1^{micro} > 10^6$ s^{-1}. In the limit, a production of 583 $\pm$ 86 G_{sol}^*/R*/s is reached (see Fig. S2). At this point, GDP release is likely to become rate-limiting.

The microscopic model is now fully parametrized (see Tables 1 and 2). Simulation results are validated by comparing the kinetics of activated G-protein production (G_{sol}^*) with both the ODE model and experiments. We observe that within statistical error, the model is consistent with experimental data for all concentrations (Fig. 4 A). The initial delay of the signals, observed in experiments, can be fully attributed to the Meta1-Meta2 equilibrium. The variability of the individual simulation trajectories is quite low, considering that they are consecutive single-molecule events of one R* activating multiple G. On the investigated timescale of 200 ms, the free-diffusion model does not exhibit significant spatial effects such as local G depletion around the location of R*. There is sufficient time for the system to equilibrate locally during G activation while the single active R* is in complex with G.

We find a mean time of 3.11 $\pm$ 2.09 ms for the overall G activation at physiological [G] = 2525 μm^{-2} (Fig. 4 A). Note that this time does not include the Meta1-Meta2 equilibrium. Decomposing the mean cycle time into individual steps, we find that the first encounter between R* and G occurs very rapidly (0.03 $\pm$ 0.03 ms). The bottlenecks for G activation are the next two steps: the conformational change required to form the reactive R*G complex (1.31 $\pm$ 1.06 ms) and the subsequent GDP release (1.61 $\pm$ 1.82 ms). We can identify the complex formation as a bottleneck with high confidence, since the uncertainty of k_1 is small (see Estimation of reaction rates in the Supporting Material). These two steps combined account for 94% of the average activation time. In the presence of
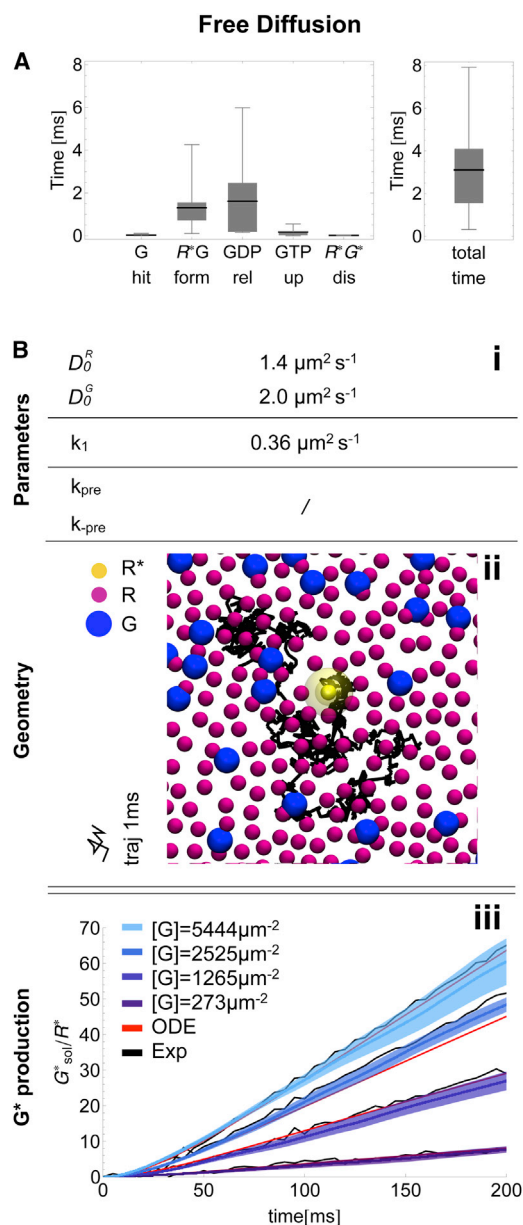
Free Diffusion

FIGURE 4 Microscopic ReaDDy simulation of the free-diffusion scenario. (*A*) Box-whisker plot of mean times required for individual reaction steps in the G activation: R* hits the first free G (*G hit*), formation of the first R*G complex (*R*G form*), first GDP release (*GDP rel*), first GTP uptake (*GTP up*) and first G* dissociation (*R*G* dis*). The cumulative time of all individual steps is depicted on the righthand side. Shown are data from 12 simulations that ran for 10 ms. (*B*) Microscopic model. (*i*) Model parameters. (*ii*) Snapshot of the simulated geometry, containing R (*purple*), R* (*yellow*), and G (*blue*). Diffusion of R* is depicted for 1 ms. Note that all particles are freely diffusing, similar to the trajectory of R*. (*iii*) G activation over time. Compared are averages of 10 ReaDDy simulations (*blue, standard error in light blue*) with the ODE model (*red*) and the experimental data (*black*). To see this figure in color, go online.

millimolar GTP, the following GTP uptake and complex dissociation reactions occur on microsecond timescales (0.14 ± 0.11 ms and 0.02 ± 0.01 ms).

Let us compare our results with the free-diffusion limit. To probe this limit, all forward reaction rates were set to infinity and all backward reaction rates to zero (i.e., a collision event between R* and G immediately leads to R* and G^*_{sol}). Under such conditions, we observe the initial G^*_{sol} production of $10,047 \pm 331$ G^*_{sol}/R*/s (see Movie S1). This value is close to previous estimates (9590 G^*_{sol}/R*/s after 10 ms of the flash, calculated from Lamb and Pugh (63)). In comparison, the measured activation rate is ~300 G^*_{sol}/R*/s (38). This emphasizes that in the free-diffusion setup, the output of the system is entirely determined by the series of chemical reactions or conformational transitions that take place during catalysis within the R*G complex.

Existence of RG precomplexes

We next considered that inactive R and G could form a nonproductive precomplex (see Eq. 4 in the reaction model (Fig. 1)). Evidence for the existence of such precomplexes has been reported in several studies (21,37,64–69), and it has been hypothesized that they are beneficial for G activation (37). Analogous to the formation of the reactive complex $R^* + G \rightleftharpoons R^*G$ (Eqs. 2 and 2.2), formation of the inactive precomplex is a bimolecular reaction that needs to be separated into its contributions of diffusional encounter and microscopic reaction (Eq. 4.2).

In the presence of inactive precomplexes, both k_1^{micro} and k_{pre}^{micro} must be parametrized. Generation of an ensemble of ReaDDy simulations to parametrize the two rates independently is computationally prohibitive. Therefore, we restrict ourselves to a limit analysis by setting both parameters to their diffusion limit, $k_1^{micro} = k_{pre}^{micro} = \infty$. This limit is equivalent to setting the macroscopic association rates in the ODE model to their Smoluchowski rate: $k_1 = k_{pre} = 1.67$ μm^2/s (see the Supporting Material for derivation). In the ReaDDy model, $k_1^{micro} = k_{pre}^{micro} = \infty$ translates to a rate of 10^8 s^{-1} due to time discretization. Apart from including the precomplex reaction, the model setup is identical to the free-diffusion setup.

The only remaining undetermined parameter is the precomplex dissociation rate, k_{-pre}, which together with the association rate determines the precomplex binding constant. We first consider using $k_{-pre} = 0.148$/s, which was estimated from recent surface plasmon resonance measurements (37). Using this rate, the G* production is virtually zero and the kinetic model is thus inconsistent with the kinetic experimental data shown in Fig. 4. This is clear from the fact that $k_{-pre} = 0.148$/s corresponds to precomplexes with a mean lifetime of 6.76 s—a factor of 3000 longer than the entire catalytic G activation found above. The situation is similar when the activated rhodopsin is precomplexed with G. Here, the first G gets activated faster, but owing to the fact that there is less G than R available, the system then becomes stuck while R* is waiting for a second free G. The time to reach a target (R*) when multiple trap

sites are around (R, to form a precomplex) has been studied by Saxton (70), who showed that traps always increase the mean time to reach the target, indicating that precomplexes cannot increase the G* production rate.

Precomplexes can only be consistent with measured kinetics if the precomplex is not too stable. ODE fitting reveals that the experimental G* production could only be reproduced with precomplex dissociation rates of at least $k_{-pre} > 11{,}200$/s (Fig. 5 A and Supporting Material). This setting leads to a ratio of 20% free G to 80% RG precomplexes. Note that $k_{-pre} = 11{,}200$/s is a lower bound to the dissociation rate; when the association rates k_1 and k_{pre} are smaller than their diffusion limits, the precomplex dissociation rate must be even larger to keep the overall G* production consistent with measured kinetics.

Existence of racks of rhodopsin dimers

Using the microscopic model, we test the molecular mobility and G* production when R is arranged in rows of dimers. For the construction of a putative R arrangement, we combine experimental observations from Fotiadis et al. (20) (racks of rhodopsin dimers) and Govardovski et al. (19) (immobile rhodopsin fractions). Both observations are consistent, because supramolecular R structures would be expected to diffuse much more slowly than single free R molecules. In our model, 80% of the R molecules are immobilized and assigned to racks of different sizes (i.e., governed by a distribution derived from Fotiadis et al. (20) (see the Supporting Material), whereas individual rhodopsins and all G proteins are freely diffusing. Note, that diffusion of G through the racks is not possible in our simulation setup.

In this geometry, a photon could activate an immobilized R that is part of a rack or an R that is freely diffusing. Position and mobility of the single R* in the simulation is consequently modeled for these two cases (see Fig. 6 A and Fig. S8 C).

The effects of immobile clustered obstacles on diffusion have been investigated in several theoretical studies (44,57,58,71). It was shown by Saxton (43) that a percolation threshold, c_p, exists when the occupied area fraction of obstacles, c, exceeds 0.332. If $c > c_p$, the obstacles separate the diffusion-accessible space into smaller subspaces. In such a scenario, the observed diffusion coefficient, D, is distance-dependent and anomalous. In our model, the immobile obstacles occupy an area fraction of $c_{im} = 0.277$ and the diffusion-accessible space is fully connected. The behavior of $\langle r^2 \rangle$ for this mixture of mobile and immobile obstacles was found to be similar to that in the free-diffusion case described above, leading to a crowding factor of $D^*_{racks} = 0.26$ (45). We reproduce these findings in our model and obtain $D^R_{racks} = 0.42 \ \mu m^2 \ s^{-1}$ and $D^G_{racks} = 0.77 \ \mu m^2 \ s^{-1}$. Note that a higher R density (e.g., the local density of 50,000 μm^{-2} reported in Fotiadis et al. (20)) would result
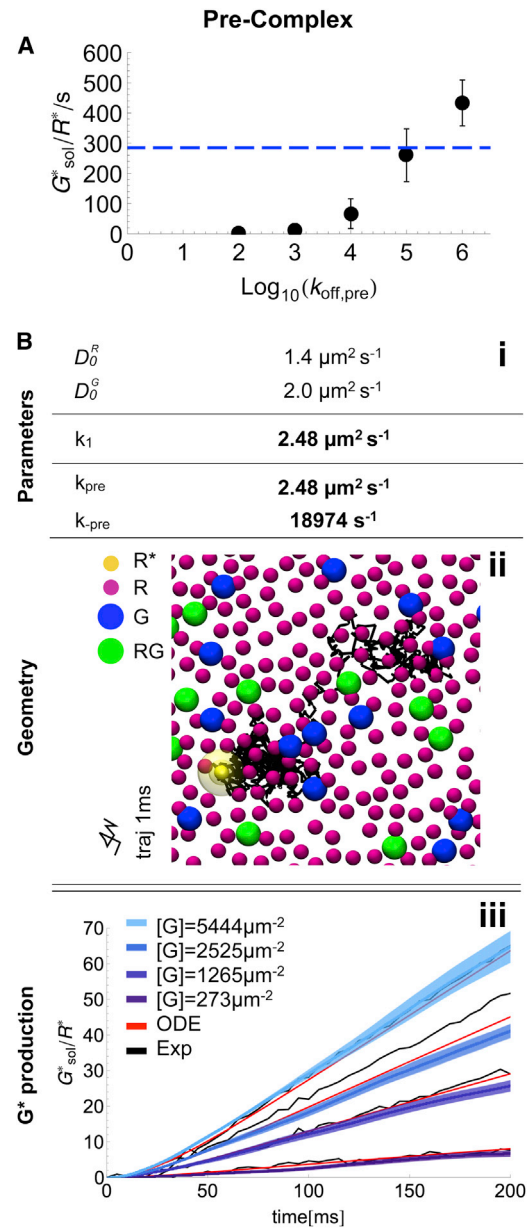

FIGURE 5 Microscopic ReaDDy simulation of the pre-complex scenario. (A) Dependence of the G* production rate on the pre-complex off rate, given that the on rate is in the diffusion limit (simulations ran for 10 ms, depicted are mean and standard error). The *dashed blue line* indicates the experimentally found G* production rate. (B) Microscopic model: (*i*) model parameters, (bold) parameters different to the free diffusion scenario. (*ii*) Snapshot of the simulated geometry, containing R (*purple*), R* (*yellow*), G (*blue*) and RG-precomplex (*green*) particles. The diffusion of R* is depicted for 1ms. Note that all particles are freely diffusing similar to the trajectory of R*. (*iii*) G activation over time. Averages of 10 ReaDDy simulations (*blue*, with standard error (*light blue*)) are compared with the ODE model (*red*) and the experimental data (*black*). To see this figure in color, go online.

in the system crossing the percolation threshold and likely showing anomalous diffusion.

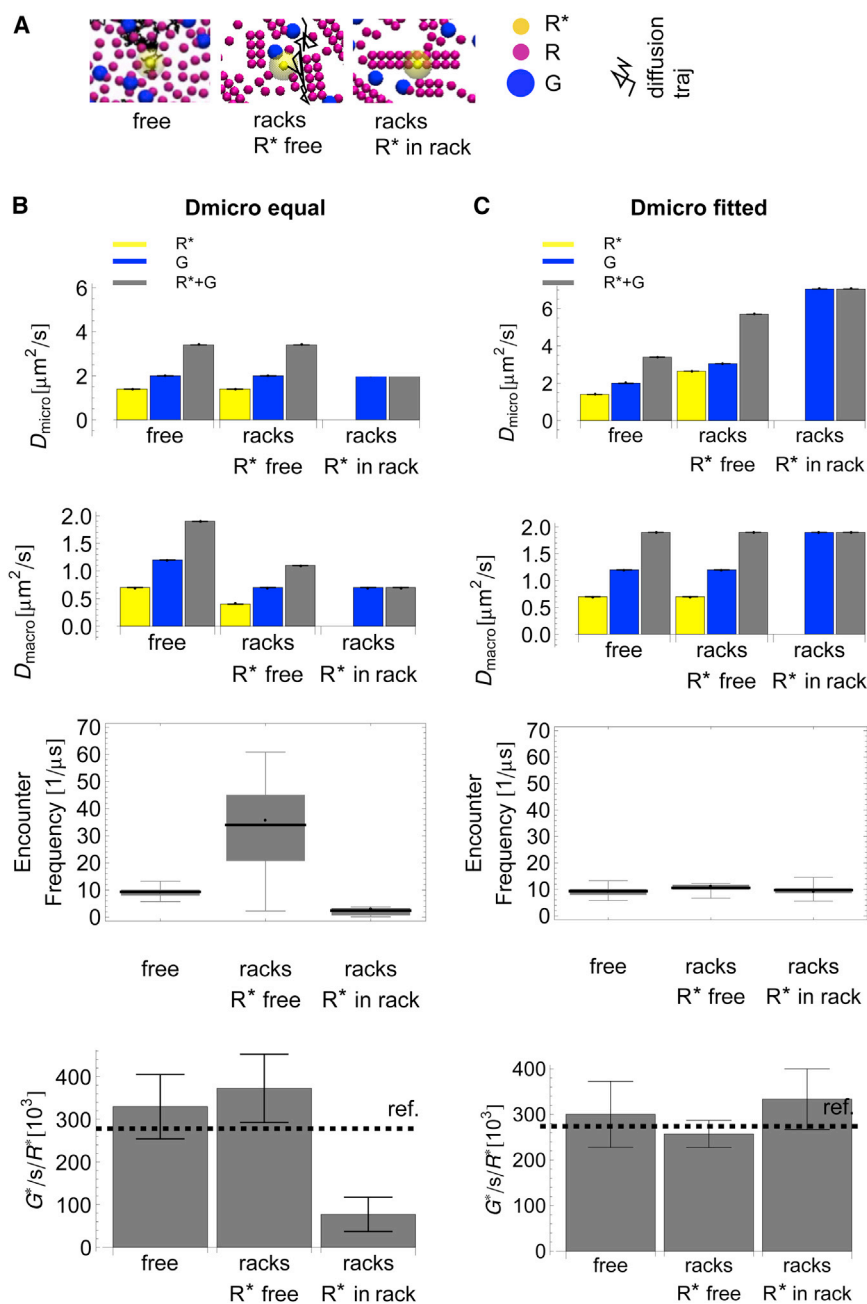It has been shown that obstacles can increase educt encounter rates (71). In our case, the R*G encounter rate

FIGURE 6 Dependence of geometry on free lipid (D_0) and apparent diffusion constant (D), encounter frequency, and G* production rate. (A) In the free-diffusion case (free), R (purple), R* (yellow), and G (blue) are all mobile. In the rack geometry, 80% of R is set as immobile in racks of dimers, whereas the other molecules diffuse freely. Here, R* can be part of the mobile fraction (racks R* free) or be part of an immobile rack (racks R* in rack). (B and C) Dependency of D_0 (first row), D (second row), R*-G encounter rate (third row), and G* production, given the geometries in A. Note the smaller scale of the y axis between the plots of free lipid and apparent diffusion constant. In B, the D_0 of the free-diffusion case is imposed for all geometries. Consequently, the crowding effects of the geometry can be seen in the apparent diffusion constant and the resulting encounter and G*-production rates. In C, the crowding effects of the geometry are compensated by imposing higher free-lipid-diffusion constants on the particles (note that the diffusion of G is set to compensate the loss of diffusion contribution from the immobilized R in the R* in rack case). As a consequence, apparent diffusion, encounter frequency, and G* production are similar in all geometries. All data shown are averages and standard errors of six simulations per scenario. Simulation timescales are 100 μs for diffusion analysis, 1 ms for encounter analysis, and 10 ms for G* catalysis. To see this figure in color, go online.

was increased threefold relative to the free-diffusion case. However, this effect was countered by slower diffusion due to obstacle-related crowding. The two effects combined result in a G* production only slightly higher than that for free diffusion (Fig. 6 B, second column).

The effects are different when R* is part of an immobile rack (Fig. 6 B, third column). Now, R* is only accessible from one side and the R*G encounter rate is solely due to the mobility of G, leading consequently to an approximately fivefold decrease in encounters compared to the number observed in free diffusion. This results in an approximately threefold decrease in G* production. In effect, the racks geometry led to a slight increase in G* catalysis when R*

is part of the mobile fraction and to a drastic decrease when R* is part of the immobile fraction.

In the next step, we reparametrized the free lipid diffusion constants, D_0, of R and G such that the effective joint diffusion constant of the free-diffusion case was reached ($D_{racks}^R + D_{racks}^G \doteq 1.9$ μm^2 s^{-1}, see Fig. 6 C, second row). For these cases, we observe the same encounter rates in all three scenarios, as well as the same G* production rate. We simulated the reparametrized rack case with the mobile R* for 200 ms and found a very good agreement with both the ODE model and the experimental data (Fig. 7 lower).

In summary, racks of rhodopsin dimers are also consistent with available kinetic data when the free lipid diffusion
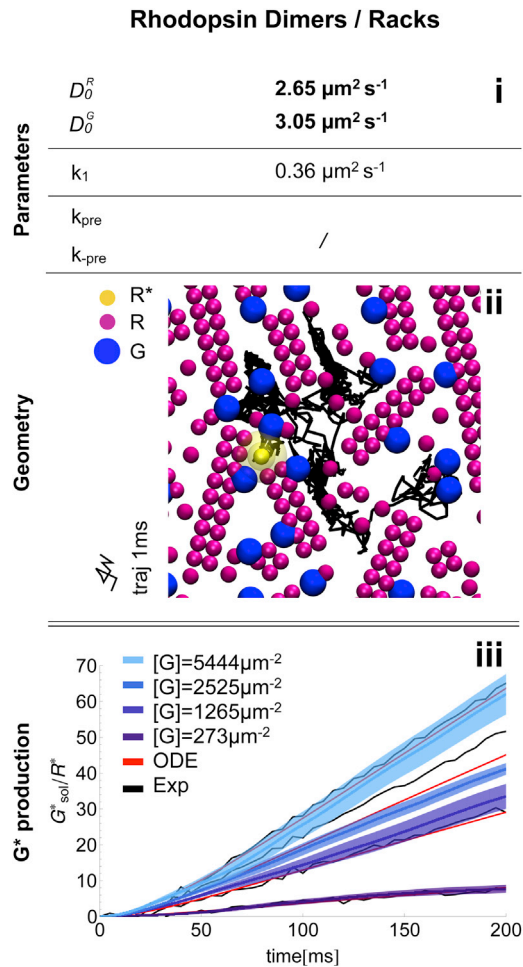
Rhodopsin Dimers / Racks

FIGURE 7 Microscopic ReaDDy simulation of the racks of rhodopsin dimers scenario. (*i*) Model parameters, highlighting (*bold*) parameters different from the free-diffusion scenario. (*ii*) Snapshot of the simulated geometry, containing R (*purple*), R* (*yellow*), and G (*blue*). Note that only G, monomeric R, and R* particles are freely diffusing. R oligomers are considered immobile. (*iii*) G activation over time. Averages of 10 ReaDDy simulations (*blue*, with standard error in *light blue*) are compared with the ODE model (*red*) and the experimental data (*black*). To see this figure in color, go online.

constants are chosen to be slightly higher than the respective values predicted by theory. The confinement conditions of racks slightly increases G* production on short timescales if the activated receptor is mobile. If R* is part of a rack (i.e., it is immobile), the rack geometry decreases G* catalysis substantially, a reduction that can only be compensated by high G-diffusion constants. Although both cases, i.e., R* mobile and R* immobile, could be made consistent with kinetic data individually, the occurrence of both scenarios on the same disk membrane would pose a challenge. Given these results, fractions of mobile and immobile rhodopsin on the same disk simultaneously would lead to a higher variance of the G* output rate, compared to the case of a homogenous geometry.

CONCLUSION

We have presented a particle-based reaction-diffusion model for light-induced, rhodopsin-mediated activation of G-proteins. Although we have chosen rod cell phototransduction as an example, for which there is a large body of experimental data, the results should be applicable to G-protein activation in general. The kinetic parameters of the model were parametrized to fit observed effective diffusion constants (see Pugh and Lamb (49)) and the extensive G-activation kinetics measurements of Heck and Hofmann (38) via an ODE model. The model was implemented in and simulated with the particle-based reaction-diffusion software ReaDDy (36). The free-diffusion parametrization could quantitatively reproduce G* production during the first 200 ms after photoactivation of R* for a set of different initial G concentrations. The main observations for this model are as follows. 1), Diffusional G-R* encounter is fast, consistent with previous predictions that the typical G* production rates (on the order of several hundred per second) are well below the diffusion limit (which would be on the order of 10,000/s). 2), Due to the high protein density in the disk membrane, the mobility of R and G is reduced compared to diffusion in a pure lipid membrane (to 0.5 D_0). 3), The conformational change required to form an active R*G complex after R* and G encounter is a bottleneck, requiring a lower millisecond timescale. 4), It is likely that GDP release from the R*G complex is the second bottleneck of the overall catalysis. Findings 3 and 4 define interesting targets for future investigations: With the advent of high-throughput computing technologies, such as special-purpose hardware (72), massive distribution computing (73–75), and Markov state models (76–79), molecular dynamics simulations are now able to describe processes on the millisecond timescale in full atomistic detail. Investigation of the detailed mechanisms of the R* + G ⇌ R*G conformational change and the GDP release in R*G → R*G + GDP would shed light on two steps that are important for the kinetics of phototransduction.

We have considered the existence of a nonproductive RG precomplex formation: R + G ⇌ RG. The existence of such precomplexes has been suggested by others (21,37,64–69). Here, we found that the existence of precomplexes is consistent with our kinetic data if they are sufficiently transient. In particular, the precomplex dissociation rate needs to be on the order of 10,000 s^{-1} or larger. This bound arises from the fact that longer-lived precomplexes would arrest the system in an inactive state dominated by the waiting time of R* for G proteins stuck at inactive rhodopsins and would consequently reduce G* production to values incompatible with the present kinetic experimental data, a case referred to as inhibition by substrate depletion in enzyme kinetics. The existence of transient RG precomplexes must be compensated by increasing the rates in the rate-limiting steps described above. In particular, the conformational change

$R^* + G \rightarrow R^*G$ could proceed somewhat faster, e.g., on the 100 μs timescale.

Please note that under no circumstances can the existence of precomplexes increase the production rate of G^*, independent of whether the activated R^* is initially precomplexed with a G or not (see Saxton (70) for a theoretical study on the effect of traps on the way to a target). If precomplexes exist, they may be due to side effects (since R^*G has interactions that form a stable complex, it is reasonable that some of these interactions are also present in RG, forming transient complexes), but precomplexes may also play a role in the regulation of signal transduction, e.g., by limiting the G^* output.

We have also considered the situation that rhodopsin forms rows of dimers (racks), as observed by Fotiadis et al. (20). One rhodopsin fraction (20%) consists of individual freely diffusing particles, and the other fraction (80%) is fixed in racks of dimers. In this model, each row of dimers is densely packed such that G cannot diffuse through it. This setup reduces the diffusional mobility of R and G by a factor of 2 more strongly than in the free-diffusion case (to $0.26D_0$), a behavior that has already been suggested in theoretical studies (61). If the single R^* is considered to be not part of a rack, the encounter rate between R^* and G is increased due to confinement compared to the free-diffusion case (also compare to Soula et al. (71)). This increase is compensated by the decreased long-range diffusion through racks. If R^* is considered to be part of a rack, the lower accessibility of R^*, its immobility, and the decrease in long-range diffusion together drastically decrease the R^*-G encounter frequency, as well as G^* formation. Note that our tested scenarios have an R density of 25,000 μm^{-2} and are therefore below the percolation threshold (i.e., the free diffusion space is fully connected). Higher R densities would likely partition the disc membrane and lead to anomalous diffusion (56,59). In summary, as has been shown in experiments (80), the diffusion conditions and the microscopic environment on the disk membrane have a strong effect on the R^*-G encounter frequency and therefore on the output of the cascade.

We find that all these effects can be compensated for if the free lipid diffusion constants (D_0) are adapted to the geometry so as to reproduce published (49) apparent diffusion constants. Compensation is possible even if R^* is immobilized completely. In this case, G-protein diffusion can make up for the encounter events alone if it is given a high free lipid diffusion constant ($2.3D_0^G$). Such values might be possible (81), especially given that the slow membrane diffusion is likely only affecting the relatively small anchor of G-proteins.

Compensation is only possible for uniform conditions on the disk membrane. In a setup in which both scenarios coexist, i.e., fractions of free and immobile R on the disk membrane, it is difficult to compensate for the effects of both conditions at the same time. Such a situation could be experimentally detected by different G^* formation rates for different individual photon events, depending on whether R^* is freely diffusing or immobile.

SUPPORTING MATERIAL

Five tables, eight figures, one movie and Supporting Methods are available at http://www.biophysj.org/biophysj/supplemental/S0006-3495(14)00690-0.

SUPPORTING CITATIONS

References (82–89) appear in the Supporting Material.

REFERENCES

1. Kruse, A. C., A. M. Ring, …, B. K. Kobilka. 2013. Activation and allosteric modulation of a muscarinic acetylcholine receptor. *Nature.* 504:101–106.

2. Hofmann, K. P., P. Scheerer, …, O. P. Ernst. 2009. A G protein-coupled receptor at work: the rhodopsin model. *Trends Biochem. Sci.* 34: 540–552.

3. Elgeti, M., A. S. Rose, …, M. Heck. 2013. Precision vs. flexibility in GPCR signaling. *J. Am. Chem. Soc.* 135:12305–12312.

4. Hofmann, K. P., C. M. Spahn, …, U. Heinemann. 2006. Building functional modules from molecular interactions. *Trends Biochem. Sci.* 31:497–508.

5. Baylor, D. A., A. L. Hodgkin, and T. D. Lamb. 1974. The electrical response of turtle cones to flashes and steps of light. *J. Physiol.* 242:685–727.

6. Lamb, T. D. 1996. Gain and kinetics of activation in the G-protein cascade of phototransduction. *Proc. Natl. Acad. Sci. USA.* 93:566–570.

7. Hamer, R., S. Nicholas, D. Tranchina, …, J. Jarvinen. 2005. Toward a unified model of vertebrate rod phototransduction. *Vis. Neurosci.* 22:417–436.

8. Invergo, B. M., D. Dell'Orco, …, J. Bertranpetit. 2014. A comprehensive model of the phototransduction cascade in mouse rod cells. *Mol. Biosyst.* 10:1481–1489.

9. Lamb, T. D. 1994. Stochastic simulation of activation in the G-protein cascade of phototransduction. *Biophys. J.* 67:1439–1454.

10. Felber, S., H. P. Breuer, …, K. P. Hofmann. 1996. Stochastic simulation of the transducin GTPase cycle. *Biophys. J.* 71:3051–3063.

11. Andreucci, D., P. Bisegna, …, E. DiBenedetto. 2003. Mathematical model of the spatio-temporal dynamics of second messengers in visual transduction. *Biophys. J.* 85:1358–1376.

12. Caruso, G., H. Khanal, …, E. DiBenedetto…, 2005. Mathematical and computational modelling of spatio-temporal signalling in rod phototransduction. *Syst. Biol.* 152:119–137.

13. Caruso, G., P. Bisegna, …, E. DiBenedetto. 2006. Modeling the role of incisures in vertebrate phototransduction. *Biophys. J.* 91:1192–1212.

14. Straube, R., and M. J. Ward. 2009. An asymptotic analysis of intracellular signaling gradients arising from multiple small compartments. *SIAM J. Appl. Math.* 70:248–269.

15. Coombs, D., R. Straube, and M. Ward. 2009. Diffusion on a sphere with localized traps: mean first passage time, eigenvalue asymptotics, and Fekete points. *SIAM J. Appl. Math.* 70:302–332.

16. Pillay, S., M. J. Ward, ..., T. Kolokolnikov. 2009. An asymptotic analysis of the mean first passage time for narrow escape problems: Part I: Two-dimensional domains. *Multiscale Model. Simul.* 8:803–835.

17. Cheviakov, A. F., M. J. Ward, and R. Straube. 2009. An asymptotic analysis of the mean first passage time for narrow escape problems: Part II: The sphere. *Multiscale Model. Simul.* 8:836–870.

18. Buzhynskyy, N., C. Salesse, and S. Scheuring. 2011. Rhodopsin is spatially heterogeneously distributed in rod outer segment disk membranes. *J. Mol. Recognit.* 24:483–489.

19. Govardovskii, V. I., D. A. Korenyak, ..., L. V. Zueva. 2009. Lateral diffusion of rhodopsin in photoreceptor membrane: a reappraisal. *Mol. Vis.* 15:1717–1729.

20. Fotiadis, D., Y. Liang, ..., K. Palczewski. 2003. Atomic-force microscopy: rhodopsin dimers in native disc membranes. *Nature.* 421: 127–128.

21. Dell'Orco, D., and H. Schmidt. 2008. Mesoscopic Monte Carlo simulations of stochastic encounters between photoactivated rhodopsin and transducin in disc membranes. *J. Phys. Chem. B.* 112:4419–4426.

22. Byrne, M. J., M. N. Waxham, and Y. Kubota. 2010. Cellular dynamic simulator: an event driven molecular simulation environment for cellular physiology. *Neuroinformatics.* 8:63–82.

23. Sanford, C., M. L. Yip, ..., J. Parkinson. 2006. Cell^{++}—simulating biochemical pathways. *Bioinformatics.* 22:2918–2925.

24. Takahashi, K., S. Tanase-Nicola, and P. R. ten Wolde. 2010. Spatiotemporal correlations can drastically change the response of a MAPK pathway. *Proc. Natl. Acad. Sci. USA.* 107:2473–2478.

25. van Zon, J. S., and P. R. ten Wolde. 2005. Green's-function reaction dynamics: a particle-based approach for simulating biochemical networks in time and space. *J. Chem. Phys.* 123:234910.

26. van Zon, J. S. J., and P. R. P. ten Wolde. 2005. Simulating biochemical networks at the particle level and in time and space: Green's function reaction dynamics. *Phys. Rev. Lett.* 94:128103.

27. Yachie-Kinoshita, A., T. Nishino, ..., M. Tomita. 2010. A metabolic model of human erythrocytes: practical application of the E-Cell Simulation Environment. *J. Biomed. Biotechnol.* 2010:642420.

28. Klann, M. T., A. Lapin, and M. Reuss. 2011. Agent-based simulation of reactions in the crowded and structured intracellular environment: influence of mobility and location of the reactants. *BMC Syst. Biol.* 5:71.

29. Klann, M., H. Koeppl, and M. Reuss. 2012. Spatial modeling of vesicle transport and the cytoskeleton: the challenge of hitting the right road. *PLoS ONE.* 7:e29645.

30. Stiles, J. R., D. Van Helden, ..., M. M. Salpeter. 1996. Miniature endplate current rise times less than 100 microseconds from improved dual recordings can be modeled with passive acetylcholine diffusion from a synaptic vesicle. *Proc. Natl. Acad. Sci. USA.* 93:5747–5752.

31. Kerr, R. A., T. M. Bartol, ..., J. R. Stiles. 2008. Fast Monte Carlo simulation methods for biological reaction-diffusion systems in solution and on surfaces. *SIAM J. Sci. Comput.* 30:3126.

32. Ridgway, D., G. Broderick, ..., M. J. Ellison. 2008. Coarse-grained molecular simulation of diffusion and reaction kinetics in a crowded virtual cytoplasm. *Biophys. J.* 94:3748–3759.

33. Andrews, S. S., and D. Bray. 2004. Stochastic simulation of chemical reactions with spatial resolution and single molecule detail. *Phys. Biol.* 1:137–151.

34. Andrews, S., N. Addy, and R. Brent. 2010. Detailed simulations of cell biology with smoldyn 2.1. *PLoS Computational Biol.* 6:e1000705.

35. Gruenert, G., B. Ibrahim, ..., P. Dittrich. 2010. Rule-based spatial modeling with diffusing, geometrically constrained molecules. *BMC Bioinformatics.* 11:307.

36. Schöneberg, J., and F. Noé. 2013. ReaDDy—a software for particle-based reaction-diffusion dynamics in crowded cellular environments. *PLoS ONE.* 8:e74261.

37. Dell'Orco, D., and K.-W. Koch. 2011. A dynamic scaffolding mechanism for rhodopsin and transducin interaction in vertebrate vision. *Biochem. J.* 440:263–271.

38. Heck, M., and K. P. Hofmann. 2001. Maximal rate and nucleotide dependence of rhodopsin-catalyzed transducin activation: initial rate analysis based on a double displacement mechanism. *J. Biol. Chem.* 276:10000–10009.

39. Okada, T., M. Sugihara, ..., V. Buss. 2004. The retinal conformation and its environment in rhodopsin in light of a new 2.2 Å crystal structure. *J. Mol. Biol.* 342:571–583.

40. Choe, H.-W., Y. J. Kim, ..., O. P. Ernst. 2011. Crystal structure of metarhodopsin II. *Nature.* 471:651–655.

41. Lambright, D. G., J. Sondek, ..., P. B. Sigler. 1996. The 2.0 Å crystal structure of a heterotrimeric G protein. *Nature.* 379:311–319.

42. Rasmussen, S. G. F., B. T. DeVree, ..., B. K. Kobilka. 2011. Crystal structure of the $\beta2$ adrenergic receptor-Gs protein complex. *Nature.* 477:549–555.

43. Saxton, M. J. 1987. Lateral diffusion in an archipelago. The effect of mobile obstacles. *Biophys. J.* 52:989–997.

44. Saxton, M. J. 1989. Lateral diffusion in an archipelago. Distance dependence of the diffusion coefficient. *Biophys. J.* 56:615–622.

45. Saxton, M. J. 1990. Lateral diffusion in a mixture of mobile and immobile particles. A Monte Carlo study. *Biophys. J.* 58:1303–1306.

46. Saxton, M. J. 1993. Lateral diffusion in an archipelago. Dependence on tracer size. *Biophys. J.* 64:1053–1062.

47. Metzler, R., and T. F. Nonnenmacher. 2002. Space-and time-fractional diffusion and wave equations, fractional Fokker-Planck equations, and physical motivation. *Chem. Phys.* 284:67–90.

48. Saxton, M. J. 2007. A biological interpretation of transient anomalous subdiffusion. I. Qualitative model. *Biophys. J.* 92:1178–1191.

49. Pugh, Jr., E. N., and T. D. Lamb. 1993. Amplification and kinetics of the activation steps in phototransduction. *Biochim. Biophys. Acta.* 1141:111–149.

50. Liebman, P. A., and G. Entine. 1974. Lateral diffusion of visual pigment in photorecptor disk membranes. *Science.* 185:457–459.

51. Takezoe, H., and H. Yu. 1981. Lateral diffusion of photopigments in photoreceptor disk membrane vesicles by the dynamic Kerr effect. *Biochemistry.* 20:5275–5281.

52. Gupta, B. D., and T. P. Williams. 1990. Lateral diffusion of visual pigments in toad (*Bufo marinus*) rods and in catfish (*Ictalurus punctatus*) cones. *J. Physiol.* 430:483–496.

53. Wang, Q., X. Zhang, ..., T. G. Wensel. 2008. Activation-dependent hindrance of photoreceptor G protein diffusion by lipid microdomains. *J. Biol. Chem.* 283:30015–30024.

54. Najafi, M., M. Haeri, ..., P. Calvert. 2012. Impact of signaling microcompartment geometry on GPCR dynamics in live retinal photoreceptors. *J. Gen. Physiol.* 140:249–266.

55. Salom, D., D. T. Lodowski, ..., K. Palczewski. 2006. Crystal structure of a photoactivated deprotonated intermediate of rhodopsin. *Proc. Natl. Acad. Sci. USA.* 103:16123–16128.

56. Saxton, M. J. 1994. Anomalous diffusion due to obstacles: a Monte Carlo study. *Biophys. J.* 66:394–401.

57. Javanainen, M., H. Hammaren, ..., I. Vattulainen. 2013. Anomalous and normal diffusion of proteins and lipids in crowded lipid membranes. *Faraday Discuss.* 161:397–417, discussion 419–459.

58. Ehrig, J., E. P. Petrov, and P. Schwille. 2011. Near-critical fluctuations and cytoskeleton-assisted phase separation lead to subdiffusion in cell membranes. *Biophys. J.* 100:80–89.

59. Berry, H., and H. Chaté. 2014. Anomalous diffusion due to hindering by mobile obstacles undergoing Brownian motion or Orstein-Uhlenbeck processes. *Phys. Rev. E Stat. Nonlin. Soft Matter Phys.* 89:022708.

60. Klafter, J., and I. M. Sokolov. 2005. Anomalous diffusion spreads its wings. *Physics world.* August:29–32.

61. Saxton, M. J., and J. C. Owicki. 1989. Concentration effects on reactions in membranes: rhodopsin and transducin. *Biochim. Biophys. Acta.* 979:27–34.

62. Johnston, C. A., and D. P. Siderovski. 2007. Receptor-mediated activation of heterotrimeric G-proteins: current structural insights. *Mol. Pharmacol.* 72:219–230.

63. Lamb, T. D., and E. N. Pugh, Jr. 1992. A quantitative account of the activation steps involved in phototransduction in amphibian photoreceptors. *J. Physiol.* 449:719–758.

64. Alves, I. D., G. F. J. Salgado, …, V. J. Hruby. 2005. Phosphatidylethanolamine enhances rhodopsin photoactivation and transducin binding in a solid supported lipid bilayer as determined using plasmon-waveguide resonance spectroscopy. *Biophys. J.* 88:198–210.

65. Dell'Orco, D. 2013. A physiological role for the supramolecular organization of rhodopsin and transducin in rod photoreceptors. *FEBS Lett.* 587:2060–2066.

66. Fanelli, F., and D. Dell'Orco. 2005. Rhodopsin activation follows precoupling with transducin: inferences from computational analysis. *Biochemistry.* 44:14695–14700.

67. Fanelli, F., and D. Dell'orco. 2008. Dark and photoactivated rhodopsin share common binding modes to transducin. *FEBS Lett.* 582:991–996.

68. Hamm, H. E., D. Deretic, …, B. Kohl. 1987. Mechanism of action of monoclonal antibodies that block the light activation of the guanyl nucleotide-binding protein, transducin. *J. Biol. Chem.* 262:10831–10838.

69. Kim, T. Y., H. Uji-i, …, U. Alexiev. 2009. Monitoring the interaction of a single G-protein key binding site with rhodopsin disk membranes upon light activation. *Biochemistry.* 48:3801–3803.

70. Saxton, M. J. 2008. A biological interpretation of transient anomalous subdiffusion. II. Reaction kinetics. *Biophys. J.* 94:760–771.

71. Soula, H., B. Caré, …, H. Berry. 2013. Anomalous versus slowed-down Brownian diffusion in the ligand-binding equilibrium. *Biophys. J.* 105:2064–2073.

72. Shaw, D. E., P. Maragakis, …, W. Wriggers. 2010. Atomic-level characterization of the structural dynamics of proteins. *Science.* 330:341–346.

73. Shirts, M., and V. S. Pande. 2000. COMPUTING: screen savers of the world unite! *Science.* 290:1903–1904.

74. Harvey, M. J., G. Giupponi, and G. D. Fabritiis. 2009. ACEMD: accelerating biomolecular dynamics in the microsecond time scale. *J. Chem. Theory Comput.* 5:1632–1639.

75. Eastman, P., M. S. Friedrichs, …, V. S. Pande. 2012. OpenMM 4: a reusable, extensible, hardware independent library for high performance molecular simulation. *J. Chem. Theory Comput.* 9:461–469.

76. Swope, W. C., J. W. Pitera, and F. Suits. 2004. Describing protein folding kinetics by molecular dynamics simulations: 1. Theory. *J. Phys. Chem. B.* 108:6571–6581.

77. Schütte, C., A. Fischer, …, P. Deuflhard. 1999. A direct approach to conformational dynamics based on hybrid Monte Carlo. *J. Comput. Phys.* 151:146–168.

78. Noé, F., I. Horenko, …, J. C. Smith. 2007. Hierarchical analysis of conformational dynamics in biomolecules: transition networks of metastable states. *J. Chem. Phys.* 126:155102.

79. Noé, F., C. Schütte, …, T. R. Weikl. 2009. Constructing the equilibrium ensemble of folding pathways from short off-equilibrium simulations. *Proc. Natl. Acad. Sci. USA.* 106:19011–19016.

80. Calvert, P. D., V. I. Govardovskii, …, C. L. Makino. 2001. Membrane protein diffusion sets the speed of rod phototransduction. *Nature.* 411:90–94.

81. Chang, C. H., H. Takeuchi, …, S. Ohnishi. 1981. Lateral mobility of erythrocyte membrane proteins studied by the fluorescence photobleaching recovery technique. *J. Biochem.* 90:997–1004.

82. Segel, I. H. 1975. Enzyme Kinetics. John Wiley & Sons, New York.

83. Kühn, H., N. Bennett, …, M. Chabre. 1981. Interactions between photoexcited rhodopsin and GTP-binding protein: kinetic and stoichiometric analyses from light-scattering changes. *Proc. Natl. Acad. Sci. USA.* 78:6873–6877.

84. Heck, M., A. Pulvermüller, and K. P. Hofmann. 2000. Light scattering methods to monitor interactions between rhodopsin-containing membranes and soluble proteins. *Methods Enzymol.* 315:329–347.

85. Parkes, J. H., and P. A. Liebman. 1984. Temperature and pH dependence of the metarhodopsin I-metarhodopsin II kinetics and equilibria in bovine rod disk membrane suspensions. *Biochemistry.* 23:5054–5061.

86. Jäger, S., I. Szundi, …, D. S. Kliger. 1998. Effects of pH on rhodopsin photointermediates from lumirhodopsin to metarhodopsin II. *Biochemistry.* 37:6998–7005.

87. Seitz, H. R., M. Heck, …, A. Seelig. 1999. Molecular determinants of the reversible membrane anchorage of the G-protein transducin. *Biochemistry.* 38:7950–7960.

88. Kung, C. E., and J. K. Reed. 1986. Microviscosity measurements of phospholipid bilayers using fluorescent dyes that undergo torsional relaxation. *Biochemistry.* 25:6114–6121.

89. Erban, R., and S. J. Chapman. 2009. Stochastic modelling of reaction-diffusion processes: algorithms for bimolecular reactions. *Phys. Biol.* 6:046001.

Supporting Information

for

Explicit Spatio-Temporal Simulation of Receptor-G Protein Coupling in Rod Cell Disk Membranes

Johannes Schöneberg[1], Martin Heck[2], Klaus-Peter Hofmann[2], Frank Noé[1]

[1] Department of Mathematics, Computer Science and Bioinformatics, FU Berlin, Arnimallee 6, 14195 Berlin, Germany
[2] Institut für Medizinische Physik und Biophysik, Charité - Universitätsmedizin Berlin, Charitéplatz 1, 10117 Berlin, Germany

Table S1: Kinetic parameters of G activation

Parameter		Kinetic definition [a]	Value [b]
$\dfrac{V_{max}}{R*}$	(forward) turnover number	$\dfrac{k_2 k_4}{(k_2 + k_4)}$	$594 \pm 17\ \mathrm{s}^{-1}$
K_m^G	Michaelis constant for Gt	$\dfrac{k_4(k_{-1} + k_2)}{k_1(k_2 + k_4)}$	$2182 \pm 110\ \mu\mathrm{m}^{-2}$
K_m^{GTP}	Michaelis constant for GTP	$\dfrac{k_2(k_{-3} + k_4)}{k_3(k_2 + k_4)}$	$231 \pm 10\ \mu\mathrm{M}$
K_d^G	dissociation constant for Gt	$\dfrac{k_{-1}}{k_1}$	$534 \pm 257\ \mu\mathrm{m}^{-2}$
K_d^{GDP}	dissociation constant for GDP	$\dfrac{k_2}{k_{-2}}$	$274 \pm 37\ \mu\mathrm{M}$

[a] see (1) for derivation; for assignment of the individual rate constants see Fig. 1A and Table 1.
[b] Values are taken from (2) and represent the experimentally obtained values corrected for the fraction of active receptor relative to the total amount of light-activated rhodopsin.

Table S2: Initial concentrations of the reactants in ODE-fitting

Species	Initial concentration
$[M1]_n^0$	$5.7\ \mu\mathrm{m}^{-2}$
$[R*]_n^0$	0
$[G]_1^0$	$273\ \mu\mathrm{m}^{-2}$ (a)
$[G]_2^0$	$1265\ \mu\mathrm{m}^{-2}$ (a)
$[G]_3^0$	$2525\ \mu\mathrm{m}^{-2}$ (a)
$[G]_4^0$	$5444\ \mu\mathrm{m}^{-2}$ (a)
$[G]_5^0$	$655\ \mu\mathrm{m}^{-2}$
$[G]_6^0$	$2160\ \mu\mathrm{m}^{-2}$
$[G]_7^0$	$3706\ \mu\mathrm{m}^{-2}$
$[R*G]_n^0$	0
$[R*G_0]_n^0$	0
$[R*G*]_n^0$	0
$[G*]_n^0$	0
$[G*_{sol}]_n^0$	0

(a) G concentrations also used for ReaDDy

Table S3: Initial estimation of selected rate constants

Rate constant	Description	Initial estimation
k_1	Rate of R*G complex formation	$0.27\ \mu m^2 s^{-1} < k_1 < 0.36\ \mu m^2 s^{-1}$
k_{-1}	Rate of R*G complex dissociation	$145\ s^{-1} < k_{-1} < 192\ s^{-1}$
k_2	Rate of GDP release from R*G complex	$> 594\ s^{-1}$
k_{-2}	Rate of GDP uptake by R*G complex	$> 2.2\ \mu M^{-1} s^{-1}$
k_3	Rate of GTP uptake by R*G complex	$> 2.57\ \mu M^{-1} s^{-1}$
k_{-3}	Rate of GTP release from R*G* complex	$< 594\ s^{-1}$
k_4	Rate of R*G* complex dissociation	$> 594\ s^{-1}$

Table S4: Estimation of rate constants

Rate constant	Set A	Set B
k_{M2}	$35.4\ s^{-1}$	
k_{-M2}	$14.4\ s^{-1}$	
k_1	$0.36\ \mu m^2 s^{-1}$	$0.27\ \mu m^2 s^{-1}$
k_{-1}	200	140
k_2	$600\ s^{-1}$	$60000\ s^{-1}$
$k_{-2}^{GDP} = k_{-2}\ [GDP]$	$2.6\ \mu M^{-1} s^{-1}\ [GDP]$	$260\ \mu M^{-1} s^{-1}\ [GDP]$
$k_{3}^{GTP} = k_3\ [GTP]$	$2.6\ \mu M^{-1} s^{-1}\ [GTP]$	$5.1\ \mu M^{-1} s^{-1}\ [GTP]$
k_{-3}	$600\ s^{-1}$	
k_4	$60000\ s^{-1}$	$600\ s^{-1}$
k_{-4}	$0\ s^{-1}$	
k_{sol}	$10000\ s^{-1}$	
k_{-sol}	$0\ s^{-1}$	

Reaction rates derived from ODE-fitting for the reaction system given in Eqs. (1)-(3) in Fig. 1.

Estimation of the rate constants and ODE-model

Activation of Gt is accompanied *in vitro* by a complete release of the active Gtα-subunit and

a partial release of the Gtβγ-subunit from the disk membranes. Accordingly, light-induced activation of Gt can be monitored in real time by probing the resulting loss of mass of the disk vesicles as a decrease of near infrared light scattering ("dissociation signal"; (2-4)). In a previous study, kinetic parameters for the individual steps of Gt activation (Table S1) were quantified by a rate analysis of dissociation signals titrated with Gt, GTP and GDP (2). In the following, these kinetic parameters were used for a rough initial estimation of the individual rate constants.

Initial estimation of k_2 and k_4

Solving the definition equation of the turnover number $\dfrac{V_{max}}{R^*} = \dfrac{k_2 k_4}{\left(k_2 + k_4\right)} = 594 \text{ s}^{-1}$ for k_2 and k_4, respectively, yields:

$$k_2 = \frac{k_4\, 594 s^{-1}}{k_4 - 594 s^{-1}} \qquad\qquad \text{(S1)}$$

and

$$k_4 = \frac{k_2\, 594 s^{-1}}{k_2 - 594 s^{-1}} \qquad\qquad \text{(S2)}$$

The lower limit for both values is thus $k_2 > 594 \text{ s}^{-1}$ and $k_4 > 594 \text{ s}^{-1}$. Importantly, the two values are mutually dependent (Eq. S1 and S2).

Initial estimation of k_1

The lower limit for k_1 (set B in Table S4) is given by (see (2) for details):

$$k_1 \geq \frac{k_{cat}}{K_m^G} = \frac{V_{max}}{R^* K_m^G} = \frac{k_1 k_2}{\left(k_{-1} + k_2\right)} = 0.272 \ \mu m^2\, s^{-1} \qquad\qquad \text{(S3)}$$

The upper limit of k_1 is estimated as follows:
With the definition of K_d^G, k_{-1} can be substituted in Eq. (S3) by $k_{-1} = k_1\, 534 \ \mu m^{-2}$, yielding after solving for k_1:

$$k_1 = \frac{0.272\, \mu m^2 s^{-1} \cdot k_2}{\left(k_2 - 145\ s^{-1}\right)} \qquad\qquad \text{(S4)}$$

With $k_2 > 594 \text{ s}^{-1}$ (see above) one obtains $k_1 < 0.36 \ \mu m^2 s^{-1}$ (set A in Table S4)

Initial estimation of k_{-1}

Solving the definition of $K_d^G = \dfrac{k_{-1}}{k_1} = 534\, \mu m^{-2}$ for k_{-1} yields

$$k_{-1} = k_1\, 534 \ \mu m^{-2} \qquad\qquad \text{(S5)}$$

With the limiting values for k_1 one obtains

$145\ \text{s}^{-1} < k_{-1} < 192\ \text{s}^{-1}$.

Initial estimation of k_{-2}

Solving the definition of $K_d^{GDP} = \dfrac{k_2}{k_{-2}} = 274\ \mu M$ for k_{-2} yields

$$k_{-2} = \frac{k_2}{274\ \mu M} \tag{S6}$$

With $k_2 > 594\ \text{s}^{-1}$ one obtains

$k_{-2} > 2.2\ \mu\text{M}^{-1}\ \text{s}^{-1}$

Initial estimation of k_3

Analogous to the estimation of the lower limit for k_1 (see above), the lower limit for k_3 is given by:

$$k_3 \geq \frac{k_{cat}}{K_m^{GTP}} = \frac{V_{max}}{R * K_m^{GTP}} = 2.57\ \mu\text{M}^{-1}\ \text{s}^{-1}$$

Initial estimation of k_{-3}

A limiting value for k_{-3} can be obtained from the fact, that the Michaelis constant for GTP (K_m^{GTP}) confine the upper limit of the dissociation constant for GTP (K_d^{GTP}):

$$K_d^{GTP} = \frac{k_{-3}}{k_3} \leq K_m^{GTP} \tag{S7}$$

Solving Eq. S7 for k_{-3} yields

$$k_{-3} \leq K_m^{GTP}\ k_3$$

and with $k_3 > 2.57\ \mu\text{M}^{-1}\ \text{s}^{-1}$ and $K_m^{GTP} = 231\ \mu M$ one obtains

$k_{-3} < 594\ \text{s}^{-1}$

Estimation of k_{-4}, k_{sol} and k_{-sol}

Dissociation of G* from R* is in the visual system followed by dissociation of G* into its subunits (GαGTP and Gβγ) and a subsequent quantitative dissociation of GαGTP from the membranes. Since the overall reaction is essentially irreversible under the experimental conditions used (2), the respective rate constants were set as given in Table S4.

Estimation of k_{M2} and k_{-M2}

Values of k_{M2} and k_{-M2} were calculated for 22°C and pH 7.4 with the equations provided by (5). The resulting values (see Table S4) are consistent with published values obtained at 20°C, pH 7.0 and pH 8.0 (6) and allow to calculate the fraction of active receptor relative to the total amount of light-activated rhodopsin (f^A; see (2)):

$$f^A = \frac{k_{M2}}{\left(k_{M2} + k_{-M2}\right)} = 0.71$$

Estimation of rate constants by ODE fitting

The classic G-protein activation scheme depicted in Fig. 1A (reactions 1-3) was used to derive a system of ordinary differential equations (ODE):

$[M1]_n' \quad = \; - k_{M2}[M1]_n + k_{-M2}[R^*]_n$

$[R^*]_n' \quad = \; k_{M2}[M1]_n - k_{-M2}[R^*]_n - k_1[R^*]_n[G]_n + k_{-1}[R^*G]_n + k_4[R^*G^*]_n$
$\qquad\qquad\; - k_{-4}[R^*]_n[G^*]_n$

$[G]_n' \quad = \; - k_1[R^*]_n[G]_n + k_{-1}[R^*G]_n$

$[R^*G]_n' \quad = \; k_1[R^*]_n[G]_n - k_{-1}[R^*G]_n - k_2[R^*G]_n + k_{-2}[GDP][R^*G_0]_n$

$[R^*G_0]_n' \quad = \; k_2[R^*G]_n - k_{-2}[GDP][R^*G_0]_n - k_3[GTP][R^*G_0]_n + k_{-3}[R^*G^*]_n$

$[R^*G^*]_n' \quad = \; k_3[GTP][R^*G_0]_n - k_{-3}[R^*G^*]_n - k_4[R^*G^*]_n + k_{-4}[R^*]_n[G^*]_n$

$[G^*]_n' \quad = \; k_4[R^*G^*]_n - k_{-4}[R^*]_n[G^*]_n - k_{sol}[G^*]_n + k_{-sol}[G^*_{sol}]_n$

$[G^*_{sol}]_n' \quad = \; k_{sol}[G^*]_n + k_{-sol}[G^*_{sol}]_n$

where the subscript of the variables (n = 1-7) identifies the individual dissociation signal used in this study. All protein concentrations are given in numbers/μm^2, and [GDP] and [GTP] denote the volume concentrations of the respective nucleotide. Due to the different concentration units, [GTP] and [GDP] are treated in the following as constants.

In order to estimate the individual rate constants, data points of seven dissociation signals were simultaneously fitted with the ODE model by applying a multiple least squares fit procedure, *i.e.* the simultaneous fit of $[G^*_{sol}]_n$ using one and the same set of rate constants. Representative dissociation signals were taken from a previous study and scaled to concentration units as described (2). The initial (t = 0) concentrations are summarized in Table S2.

In the fit procedure (Scientist Software, MicroMath), rate constants k_{-4}, k_{sol}, k_{-sol}, k_{M1} and k_{-M1}, respectively, were fixed to the values shown in Table S4. In order to include the constrains

given by the experimentally determined kinetic constants $V_{max}/R*$, K_m^G, K_m^{GTP}, K_d^G and K_d^{GDP} (Table S1), the rate constants k_{-1}, k_{-2}, k_3 and k_4, respectively, were incorporated in the fit procedure by the following equations:

$k_{-1} = k_1\,534\,\mu m^{-2}$ (see Eq. S5)

$$k_{-2} = \frac{k_2}{274\,\mu M}$$ (see Eq. S6)

$$k_4 = \frac{k_2\,594s^{-1}}{k_2 - 594s^{-1}}$$ (see Eq. S2)

Solving the definition of $K_m^{GTP} = 231\;\mu M$ (Table S1) for k_3 yields

$$k_3 = \frac{k_2\left(k_{-3} + k_4\right)}{231\mu M\left(k_2 + k_4\right)}$$

The two sets of rate constants (Table S4) were then obtained by ODE-fitting with k_1 fixed either to its upper limit ($k_1 = 0.36\;\mu m^2 s^{-1}$, set A in Table S4) or to its lower limit ($k_1 = 0.27\;\mu m^2 s^{-1}$, set B in Table S4). In both cases the rate constants k_2 and k_{-3} were allowed to vary within the limits described above. Both sets of rate constants fitted the experimental data equally well (Fig. 2 A).

In order to verify the results, another series of dissociation signals measured in the presence of 200 μM GTP (0 μM GDP, data taken from (2)) were simulated with both sets of rate constants. As seen in Fig. 2 B, the resulting traces are in good agreement with the experimental data.

Since the rate of GDP uptake by the R*G complex (i.e. rate constant k_{-2}) is not defined in the absence of GDP, the value of k_{-2} was subsequently estimated by applying the ODE fitting procedure to dissociation signals measured in the presence of 750 μM GDP and 2000 μM GDP (data taken from (2)). In this case k_{-2} was allowed to vary while all other rate constants were fixed to the values given in Table S4. The results are depicted in Fig. S1 and summarized in Table S5.

Table S5: Validation of k_{-2}

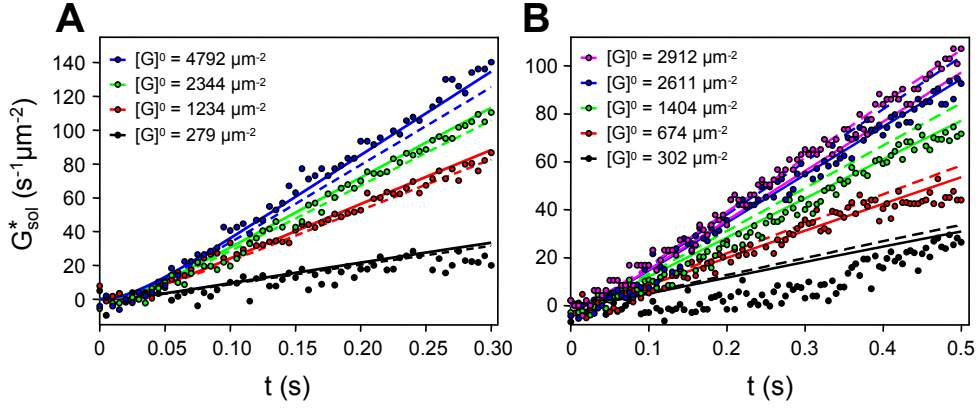|	750 μM GDP	2000 μM GDP
Set A	$k_{-2} = 2.4\;\mu M^{-1}s^{-1}$	$k_{-2} = 2.7\;\mu M^{-1}s^{-1}$
Set B	$k_{-2} = 240\;\mu M^{-1}s^{-1}$	$k_{-2} = 270\;\mu M^{-1}s^{-1}$

Fig. S1 ODE-fitting of k_{-2}. ODE-fits (lines) with k_{-2} as open parameter to representative dissociation signals (circles; taken from (2)) measured with 200 μM GTP, and 750 μM GDP (**A**) or 2000 μM GDP (**B**). (**A**) Best fits (solid lines) yield $k_{-2} = 2.4$ μM^{-1}s^{-1} (rate constant set A, Table S4) or $k_{-2} = 240$ μM^{-1}s^{-1} (rate constant set B). (**B**) Best fits (solid lines) yield $k_{-2} = 2.7$ μM^{-1}s^{-1} (rate constant set A) or $k_{-2} = 270$ μM^{-1}s^{-1} (rate constant set B). Dotted lines represent simulations with rate constant set A and $k_{-2} = 2.7$ μM^{-1}s^{-1} (A) or $k_{-2} = 2.4$ μM^{-1}s^{-1} (B).

Pre-complex case

In the case of nonproductive complex formation between inactive receptor (R) and Gt (reaction (4) in Fig. 1A; pre-complex case), the ODE model was extended as follows:

$$[Meta1]_n' = -k_{M2}[Meta1]_n + k_{-M2}[R^*]_n$$
$$[R^*]_n' = k_{M2}[MetaI]_n - k_{-M2}[R^*]_n - k_1[R^*]_n[G]_n + k_{-1}[R^*G]_n + k_4[R^*G^*]_n$$
$$- k_{-4}[R^*]_n[G^*]_n$$
$$[G]_n' = -k_1[R^*]_n[G]_n + k_{-1}[R^*G]_n - k_{pre}[R]_n[G]_n + k_{-pre}[RG]_n$$
$$[R^*G]_n' = k_1[R^*]_n[G]_n - k_{-1}[R^*G]_n - k_2[R^*G]_n + k_{-2}[GDP][R^*G_0]_n$$
$$[R^*G_0]_n' = k_2[R^*G]_n - k_{-2}[GDP][R^*G_0]_n - k_3[GTP][R^*G_0]_n + k_{-3}[R^*G^*]_n$$
$$[R^*G^*]_n' = k_3[GTP][R^*G_0]_n - k_{-3}[R^*G^*]_n - k_4[R^*G^*]_n + k_{-4}[R^*]_n[G^*]_n$$
$$[G^*]_n' = k_4[R^*G^*]_n - k_{-4}[R^*]_n[G^*]_n - k_{sol}[G^*]_n + k_{-sol}[G^*_{sol}]_n$$
$$[G^*_{sol}]_n' = k_{sol}[G^*]_n + k_{-sol}[G^*_{sol}]_n$$
$$[R]' = -k_{pre}[R]_n[G]_n + k_{-pre}[RG]_n$$
$$[RG]' = k_{pre}[R]_n[G]_n - k_{-pre}[RG]_n$$

Since the amount of RG-complex (and thus depletion of free Gt) depends on the values of k_{pre} and k_{-pre}, calculation of the initial concentrations of RG ($[RG]_n^{0\,pre}$), G ($[G]_n^{0\,pre}$) and R ($[R]_n^{0\,pre}$) were integrated in the fit procedure:

$$[RG]_n^{0\,pre} = \frac{\left(K_d^{pre} + [R]_n^0 + [G]_n^0\right) - \sqrt{\left(K_d^{pre} + [R]_n^0 + [G]_n^0\right)^2 - 4[R]_n^0[G]_n^0}}{2}$$

$$[G]_n^{0\,pre} = [G]_n^0 - [RG]_n^{0\,pre}$$

$$[R]_n^{0\,pre} = [R]_n^0 - [RG]_n^{0\,pre}$$

were $K_d^{pre} = \dfrac{k_{-pre}}{k_{pre}}$ (i.e. dissociation constant of the RG-complex), $[R]_n^0 =$ 25000 μm^{-2} and $[G]_n^0$ as given in Table S2.

In order to obtain the limiting case, values of k_{pre} and k_1 were set to the diffusion limit. To compute this, we rely on the Smoluchowski-Equation:

$$k_1^{max} = 4\pi(D_R + D_G)(r_{r,R} + r_{r,G}).$$

See Table 2 for the values of the used diffusion constants and reaction radii. We obtain k_1^{max}=0.12μm^3/s. This second order rate constant can be transformed from its volume concentration to the surface concentration necessary for our needs by the formula of (2):

$$\frac{[X]^{3D}}{[X]^{2D}} = \frac{[R]^{3D}}{[R]^{2D}}.$$

Experiments were conducted at $[R]^{3D} = 3$μM and $[R]^{2D} = 25,000$ μm^{-2}. Thus we obtain k_1^{max} = 1.67 μm^2/s.

Rates k_{pre} and k_1 were both set to k_1^{max} and k_{-pre} was allowed to vary in the ODE model (all other rate constants were fixed to the values given in Table S4, Set A). The resulting fit yields the lower limit of k_{-pre} ($k_{-pre} > 11200$ s^{-1}). Under these conditions and with native Gt concentrations (2500 - 3000 Gt μm^{-2}), about 80 % of total Gt would be initially bound to inactive receptors.
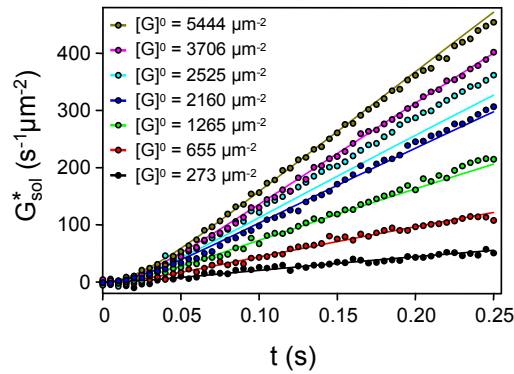

Fig. S2 ODE-fitting of k_{-pre}. ODE-fits (solid lines) with k_{-pre} as open parameter to dissociation signals (circles; measuring conditions as in Tables 1 and S2; rate constants as in Table S4). For details see text.

Model Geometry

In the reference experiment (2), disk membranes expanded to roughly spherical vesicles after having been extracted from the rod outer segment. Thus, we confine particle diffusion to a spherical surface by applying a harmonic potential along the surface normal (see Supporting Information for details). Simulating vesicle sizes found in experiment (r = 220 nm, A = 0.6 μm^2) is very CPU-intensive. Therefore, the size of the simulated vesicles was chosen such that it would host one R* on average (radius r = 120nm and surface area A = 0.18 μm^2). To mimic physiological conditions, the simulated particles comprise one R*, 4,500 R and 450 G. (See Figure 3 B for depiction).

Partice Radius Parametrization

All molecules involved in the system fall in three categories: R-type, G-type and RG-type. The R-type comprises hodopsin (R) in its inactive Meta I form (M1) and its active Meta II form (R*). The G-type contains G-proteins in its inactive (G) and active (G*) forms and the RG-type spans over all complexes formed from R-type and G-type molecules. Based on the two dimensional (2D) surface geometry of the system, all molecules are modeled as 2D disk objects. These particles collide with each other if they get closer than the sum of their collision radii (r_c). Similarly, if the distance between reacting particles is smaller than the sum of their reaction radii (r_r), a reaction can happen. In order to parametrize these radii, we rely on crystal structures (R: bovine, 1U19 (7), R*: bovine 3PQR (8); G: bovine, 1GOT (9), RG: 3SN6 (10))

Rhodopsin is a transmembrane protein, approximated by a disk with collision and reaction radii $r_c = r_r = 2.1$ nm. Note that collisions are not handled by hard space exclusions, but rather by a soft-core interaction, therefore $r_c = r_r$ does represent a nonzero reaction volume.

G is bound to disk membranes by two small lipid membrane anchors. The soluble part of the protein is modeled disk shaped with radius $r_c = 3.4$ nm, enclosing the same area as the elliptical shape of G in the crystal with axe diameters of 9 nm x 5 nm. This is the radius with which G proteins will collide with each other. R, on the other hand, can move beneath G, only colliding with the membrane anchors of G. We therefore consider two types of collision radii: $r_{c,mb}$ for membrane internal collisions and $r_{c,sol}$ for the collisions of the soluble part. The two lipid moieties form one membrane anchor with a footprint of 73 nm^2 inside the membrane (11), resulting in a collision radius of $r_{c,mb} = 0.6$ nm in our model. The reaction radius of G ($r_{r,G}$) is chosen based on the distance of the N-terminal helix in G_α to the membrane anchors (5.2 nm - 5.5 nm). The anchor and some helix residues are missing in the crystal structure that would enlarge these distances. For these reasons, we set the reaction radius conservatively to $r_{r,G} = 3$ nm (assuming a 6nm distance between anchor and N-terminal helix).

For the RG-type, we use $r_{c,RG,mb} = 2.1$ nm, i.e. radius of rhodopsin, and $r_{c,RG,sol} = 3.4$ nm, i.e. radius of soluble part of G. RG-complexes do not participate in reactions with other particles and therefore possess no reaction radius. See Fig. 2 for an illustration of the particle model and Table 2 for a summary of the data.

Particle collisions:

During simulation, repulsive particle-particle interaction potentials prevent overlaps between particles. The stiffness of these potentials is related to the timestep with which the dynamics

can be discretized. Too large timesteps in a given potential lead to large discretization errors in the time integration of the equations of motion. There is a trade-off between stiff potentials that prevent particles from overlapping and large timesteps needed to reach biologically relevant timescales. Here, we use harmonic softcore potentials:

$$U(r) = \begin{cases} 0.5\ k_{pot}(r - r_0)^2 & \text{if } r < r_0 \\ 0 & \text{else} \end{cases}, \tag{S 8}$$

with distance r between two particles, collision distance r_0 and k_{pot} = 10 kJ/mol/nm^2. The resulting repulsion potentials have a small overlap region of around $0.8nm$ between full space exclusion and no interaction, resembling the fact, that biomolecules are not solid objects and feature certain long range interactions. See the following section for details about potential Parametrization.

Potential Parametrization

The used softcore potentials allow a small overlap between particles. Therefore, in order to correctly model the desired molecular radii, we have to adjust the force constant of the repulsive term of the potential in order to arrive at a distance distribution that matches our expected particle sizes. Given the potential, we can calculate the residence probability $p(r)$ of particles in a certain distance r to one another with the following equation:

$$p(r) = 4\pi r^2 e^{\left(-\frac{U(r)}{k_B T}\right)}. \tag{S 9}$$

We define the inner core radius r_c of a particle as the region below the 25% threshold of $p(r)$, $r_c = \{r \mid p(r) = 0.25\}$ (See Figure S1). In order to set r_c to the desired particle radii given in Table 2, we have to input slightly larger radii: $r_c^{in} = r_c + 0.4nm$.

Figure S1 displays the repulsion potential in Eq. S8 for the collision distances of R-R, R-G and G-G, together with the residence probability $p(r)$ (Eq. S9) for these distances. See also Ref. (12) for details about potential parametrization.
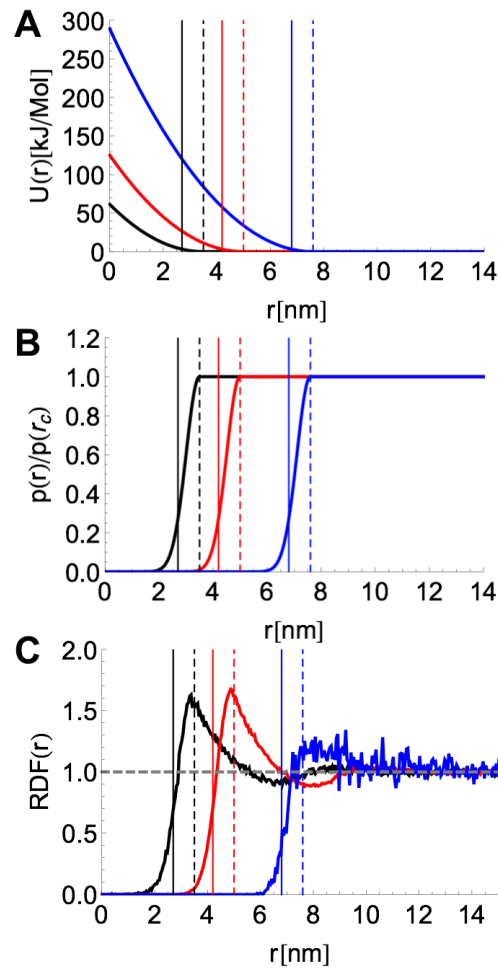
Figure S3: Input and resulting collision distances between particles. Collision distances are investigated for the following pairings: R-G (black), R-R (red) and G-G (blue). Input radii (solid vertical lines) and resulting collision radii (dashed vertical lines) are displayed in the same color code. R-G: $r^{in}_{c,R,mb} + r^{in}_{c,G,mb} = 3.5$nm, $r_{c,G,mb} = 2.7$nm; R-R: $r^{in}_{c,R,mb} + r^{in}_{c,R,mb} = 5.0$nm, $r_{c,R,mb} + r_{c,G,mb} = 4.2$nm; G-G: $r^{in}_{c,G,sol} + r^{in}_{c,G,sol} = 7.6$nm, $r_{c,R,mb} + r_{c,RGmb} = 6.8$nm. **A:** Potential governing particle interactions (Eq. S8). **B:** Residence probability of particles, calculated from Eq. S9. **C:** Radial distribution function (rdf) calculated from Monte Carlo simulation of the full sample simulation including 4500 R and 450 G particles. Depicted are averages of 100 rdfs.

Timestep Derivation

The time step was derived as described in Schöneberg and Noé 2013 (12): The size of Δt depends on the stiffness of the used potentials. In case of the current disk vesicle model, there are two potentials. A harmonic particle repulsion potential responsible for particle overlap prevention and a harmonic spherical shaped geometry potential keeping the particles on a spherical surface during the simulation. See SI Figure 2 for a depiction of the radial distribution function (RDF) of both potentials (upper left: particle repulsion, lower left: vesicle geometry). First a Monte Carlo simulation was performed in order to obtain an RDF that is not affected by time step discretization errors. This standard was then compared to BD-Simulation results of different Δt. The root mean squared error of the differences between standard and BD-simulation was computed and the largest Δt chosen that still lead to reasonable results.
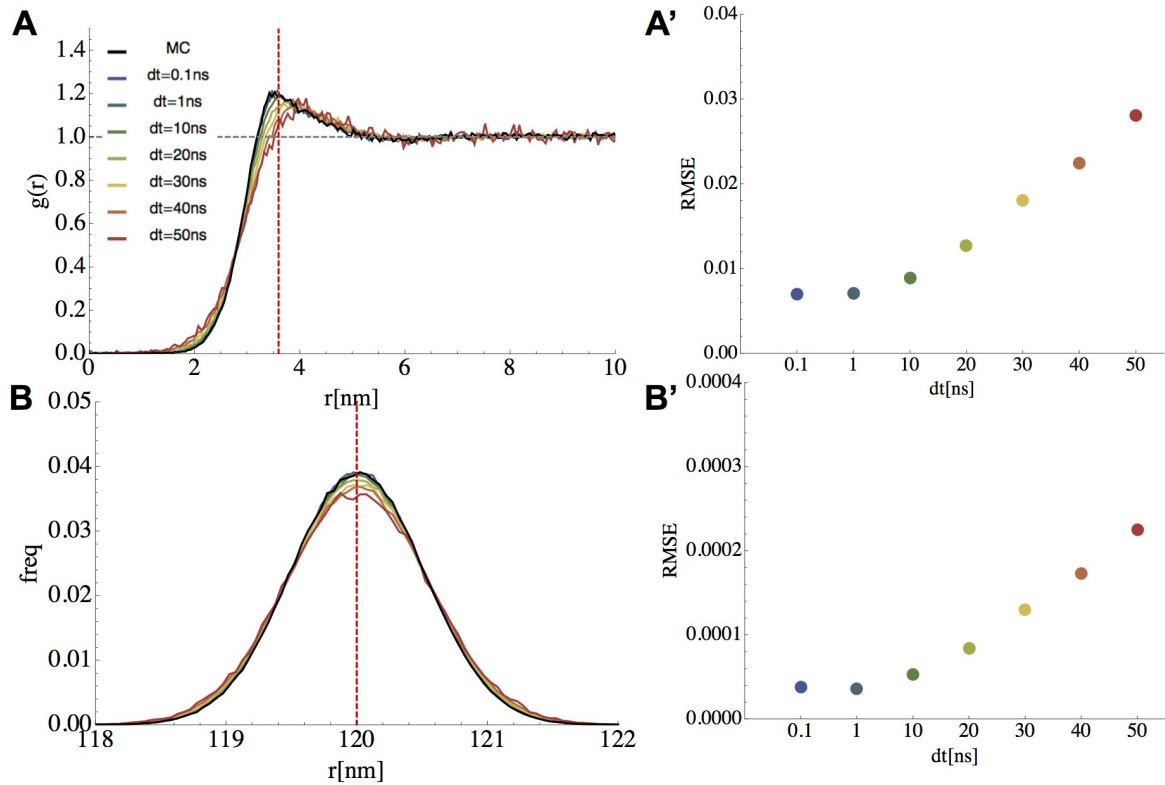
Figure S4: Influence of timestep choice on discretization error. Radial distribution function (rdf) of the two types of potentials is depicted that exist in the simulation: the pairwise repulsion potential (A) and the spherical geometry potential (B) holding the particles at 120nm distance to the origin. The black line indicates MCMC simulations that do not involve time discretization errors. The colored lines depict integration timestep length for the Brownian particle dynamics. Depicted are averages from 6 simulations per scenario. A' and B' depict the root mean squared error of the rdf results in MCMC compared with the respective time discretized Brownian particle dynamics.

Diffusion Constant Parametrization

Diffusion is a phenomenological process of large particles that perform a random motion when immersed in a solvent. Its magnitude is measured by the diffusion constant D. The Stokes-Einstein-Equation relates D to temperature T, solvent viscosity η and the radius of the immersed particle r_c, weighted by the Boltzmann-constant k_B:

$$D = \frac{k_B T}{6\pi \, \eta \, r_c}. \qquad (S10)$$

The presences of other particles may slow down the effective diffusion speed, an effect usually referred to as crowding. In monitoring the mean square displacements (msd(t) = $\langle (x_0 - x_t)^2 \rangle$) of the particles the diffusion constant can be obtained as follows:

$$D = \frac{1}{2d} \frac{d\,\langle (x_0 - x_t)^2 \rangle}{d\,t}. \qquad (S11)$$

D is proportional to the slope of the msd with d being the dimensionality of the diffusion process ($d = 2$ in this case). In crowded systems a biphasic behavior can be observed. In the first few timesteps, particles move along their mean free path with the microscopic diffusion constant D_{micro}. On longer timescales, particles collide with each other. This crowding slows down the average movement, resulting in a smaller apparent diffusion constant $D \leq D_0$.

D_0 can be derived via Eq. S10 using $\eta = 100\ cP$ at $22°C$ (13) as an estimate for the viscosity of the disk membrane. (Note that this viscosity value is assumed to be the viscosity of the lipid membrane only. Using a viscosity of a disk membrane including all proteins, Eq. S10 would result in D.) While R has a rather well-defined radius in the membrane resulting in $D_{micro}^{R,theory} = 1\mu m^2 s^{-1}$, the situation is less clear for G which has a small membrane anchor that would diffuse fast on its own ($D_0^{G,anchor,theory} = 3.6\mu m^2 s^{-1}$) but a large soluble domain whose footprint size would give rise to a much slower diffusion of ($D_0^{G,sol,theory} = 0.6\mu m^2 s^{-1}$) in the membrane. The latter value is most likely strongly underestimated, as the soluble domain is mostly affected by much less viscous cytoplasm.

Depending on the experimental method used, either D_0 or D is measured. The observed value range of D of rhodopsin is [D^R = 0.13 μm^2/s - 0.73 μm^2/s] (14-19), being measured in physiological systems at 22°C, mostly in amphibian rod cells and based on fluorescence recovery after photobleaching (FRAP) experiments. The value for G protein (D^G = 1.2 $\mu m^2 s^{-1}$) is based on an estimate of the diffusion of similar proteins and is also considered a D_{macro} value (see Ref. (20) for a review of the experiments for R and the estimate for G).

High values of D are likely to cancel any geometric effects of rhodopsin architecture while low values of D would point out geometrical effects more prominently. To do the most fair comparison between experimentally found structures, considering their ability to reproduce experimentally measured kinetics, we chose the upper limit of the available diffusion constants.

If we assume that all proteins are explicitely resolved in our simulation, given the number of particles, their macroscopic diffusion constants D and their microscopic arrangement (i.e. free diffusion of all particles, fractions of immobile particles e.g. racks of rhodopsin dimers, etc), D_0 values can be sampled by simulation that reproduce D under the given conditions on long timescales (See Figure S5 and Ref (12)).
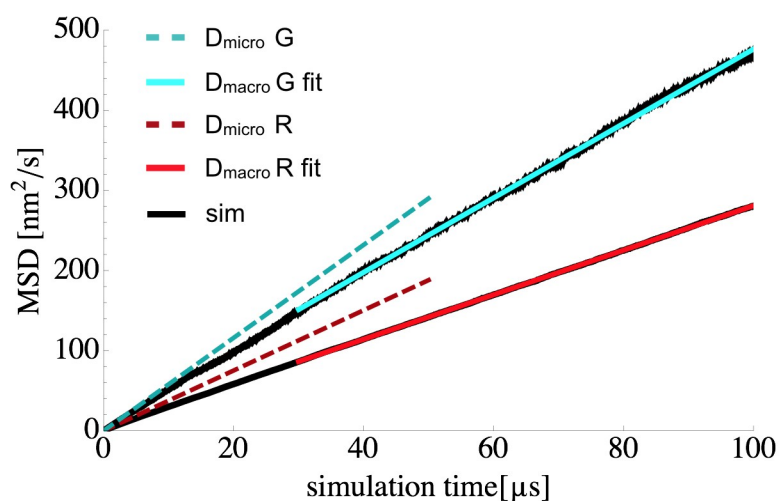
Figure S5. Parametrization of Microscopic Diffusion Constant by Simulation. The mean squared displacement (MSD) over time is depicted for R (red fits above black simulation data) and G-protein (G, blue fits above black simulation data) in the standard disc vesicle simulation. During the first timesteps, particles diffuse with D_{micro} (dashed lines). On longer time-scales, crowding slows down the particle movement (solid lines) to D_{macro}. Depicted are averages from 6 simulations.

Conversion of Reaction Rates into Reaction Probabilities

Due to time discretization in ReaDDy, all unimolecular reaction rates have to be converted in probabilities, that the reaction has happened within each timestep, provided that the requirements for a reaction are met. There are no requirements for unimolecular reactions. For bimolecular reactions, the educt particle distance has to be closer than the sum of the educt reaction radii. Rates of unimolecular reactions represent microscopic reaction rates, for bimolecular reactions, these have first to bextracted from macroscopic bimolecular rates (see next section). The reaction probability is obtained from the Poisson probability of finding at least one reaction event with rate k^{micro} in a time window Δt (12):
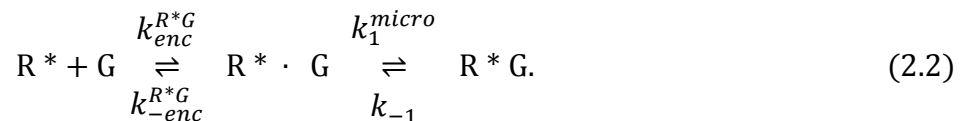
$$p(\Delta t) = 1 - \exp\left(k^{micro}\ \Delta t \right) \tag{S 12}$$

Microscopic Rate Constant Parametrization for Bimolecular Reactions

Bimolecular reactions, e.g. the initial R*G complex formation

$$R* + G \underset{k_{-1}}{\overset{k_1}{\rightleftharpoons}} R*G, \tag{first reaction in Eq. 2}$$

require a modeling step for microscopic simulations. A bimolecular reaction rate in an ODE model includes both the bimolecular rate at which the two particles form an encounter complex by diffusion k_{enc} and the unimolecular rate at which this complex overcomes the activation energy k^{micro}:

$$R* + G \underset{k_{-enc}^{R*G}}{\overset{k_{enc}^{R*G}}{\rightleftharpoons}} R* \cdot G \underset{k_{-1}}{\overset{k_1^{micro}}{\rightleftharpoons}} R*G. \tag{2.2}$$

In our simulations, diffusion is modeled explicitly. I. e. particles have to come closer than the sum of their reaction radii r_r in order to attempt a reaction with rate k_1^{micro}. In order to parametrize the simulation to the macroscopic reaction rate k_1, we must search a value for k_1^{micro} that, in conjunction with particle concentration, diffusion constants and reaction radii, leads to the effective rate k_1.

For three-dimensional diffusion, an explicit formulate exists to compute k_1^{micro} (21). For the present two-dimensional system we have to rely on sampling. k_1^{micro} is the only free parameter in the free diffusion case, and can therefore obtained by sampling G protein activation in this geometry, using the parameters from Table 1 and Table 2. The value $k_{micro} = 5000s^{-1}$ matched best the production rate of $285\ G_{sol}^*/s/R*$, the initial catalysis rate of the ODE model starting with R* (instead of with M1). See Figure 4 for a depiction of the sampling results.

This procedure is only possible for the scenarios that contain a single bimolecular reaction. In the precomplex scenario, the RG complex formation reaction introduces a second microscopic reaction rate k_{pre}^{micro} (Eq. 4.2 in Figure 1), which renders the system indeterminate.
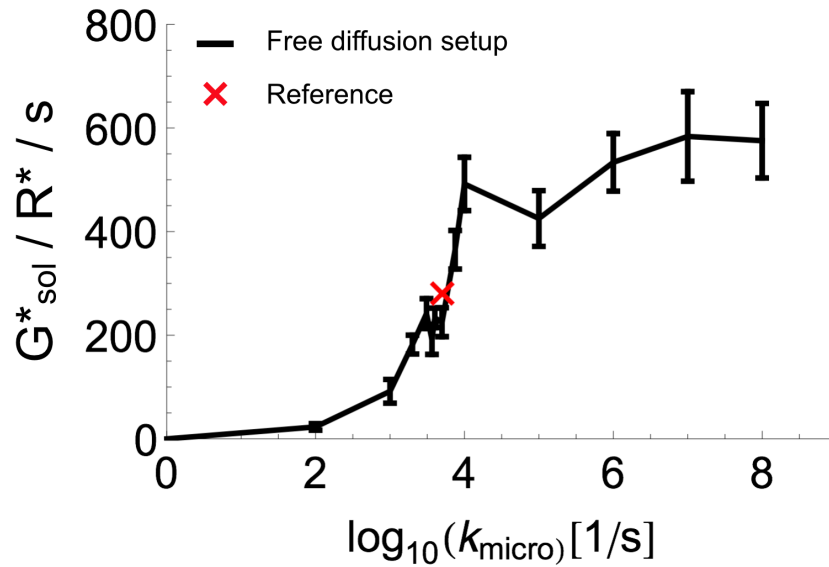
Figure S6 Parametrization of the microscopic R*+G association rate: k_1^{micro} is the single microscopic rate in the cascade that arises from a macroscopic bimolecular reaction (R* + G $\rightarrow$ R*G) in the free diffusion scenario. It is parametrized by sampling, using the standard disk vesicle geometry including reactions. The red cross indicates the number of produced G* in the experiment at [G] = 2500/µm², starting initially with R* . The plateau at large values of k_1^{micro} indicates, that in these regions, the system is no longer limited by the activation-complex reaction. Other steps in the reaction cascade are now rate-limiting. Depiced are averages and standard errors of 6 simulations per k_1^{micro}.

Time shifting method to simulate first $M1 \rightarrow R*$ **transition**

Instead of starting the simulation with an active receptor in Meta1 form, each trajectory is started in Meta2 form (R*) that capable of activating G. The shift in time, when this initial transition from Meta1 to Meta2 has happened is simulated a posteriori: For each trajectory, an ensemble of 1000 reaction times is drawn according to probability distribution $p(t) = 1 - exp(-k_{M2}t)$. Trajectories are shifted in time and averaged.
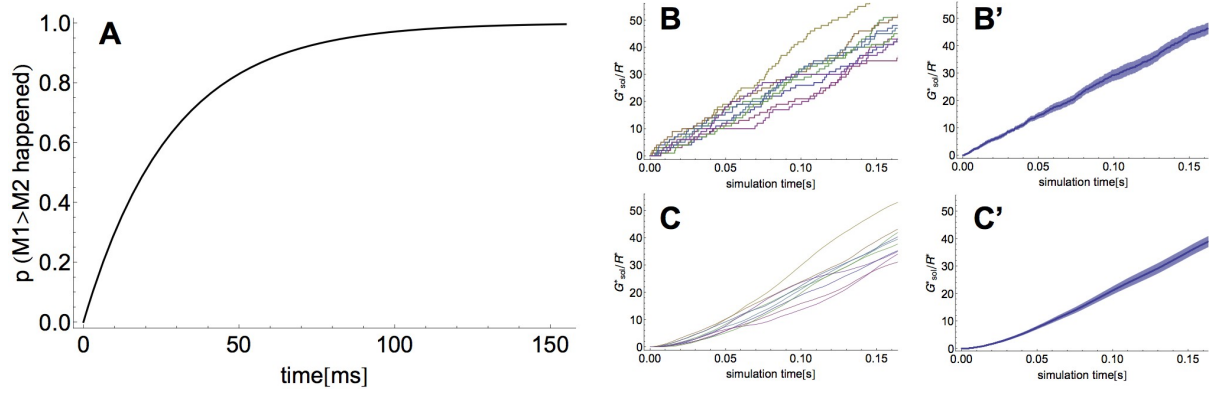
Figure S7 Time shifting method to simulate first M1 → R* transition: A: Given the time that has passed, what is the probability, that M1 has switched its state to R*. **B**: Raw G^*_{sol} production traces from simulation and their average (B'). **C**: Each raw trace, 1000 times time shifted and averaged. **C'**: Average of C.

Rack geometry structure derivation

The geometry for the rack case simulation was derived using image analysis of the microscopic image published by Fotiadis et al. 2003 (22). Rack structures that could be recognized on the image free of doubt were overlayed with lines that had the thickness of an R-dimer (Figure S8 A). The size distribution of these lines was recorded and discretized (Figure S8 B). The resulting histogram of Rack lengths was fitted with an exponential distribution, resulting a distribution of rack lengths l:

$$p_l \approx 0.261 \exp(-0.261\, l)$$

Thus, rack sizes were generated according to the following formula:

$$n_l = \left\lfloor \frac{N}{2} p_l \right\rfloor,$$

where N is the total number of R molecules and the brackets denote rounding to the next-lower integer. For the fit, the counts for rack size 0 and 1 (i.e. individual Rs and dimers) were omitted because they could not be assigned on the image free of doubt.

Using this distribution, geometries were created, based on our assumed native conditions (Table 1). 80% of the available R was assigned to racks and 20% of the available R to be monomeric and freely diffusing. R* is once considered as monomeric and once as part of a rack. See a depiction of the resulting geometries in Fig S8 C.
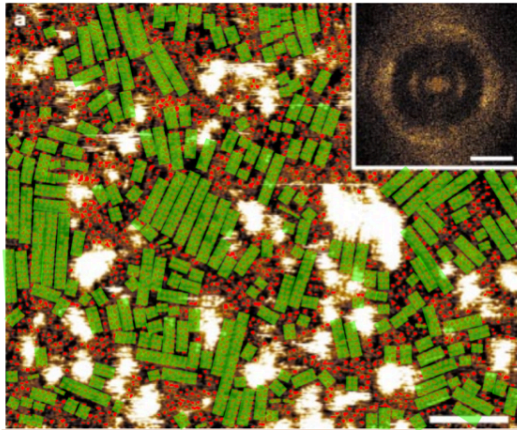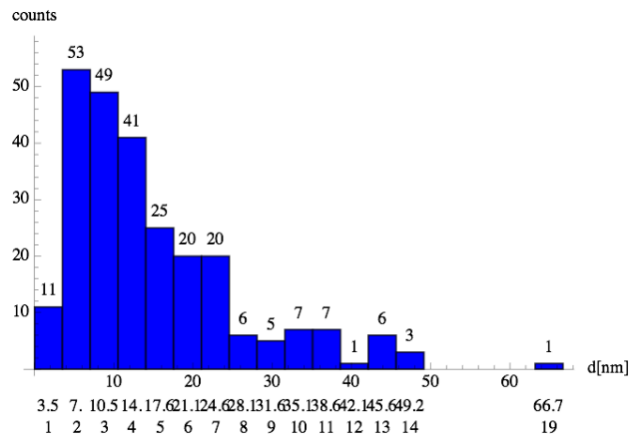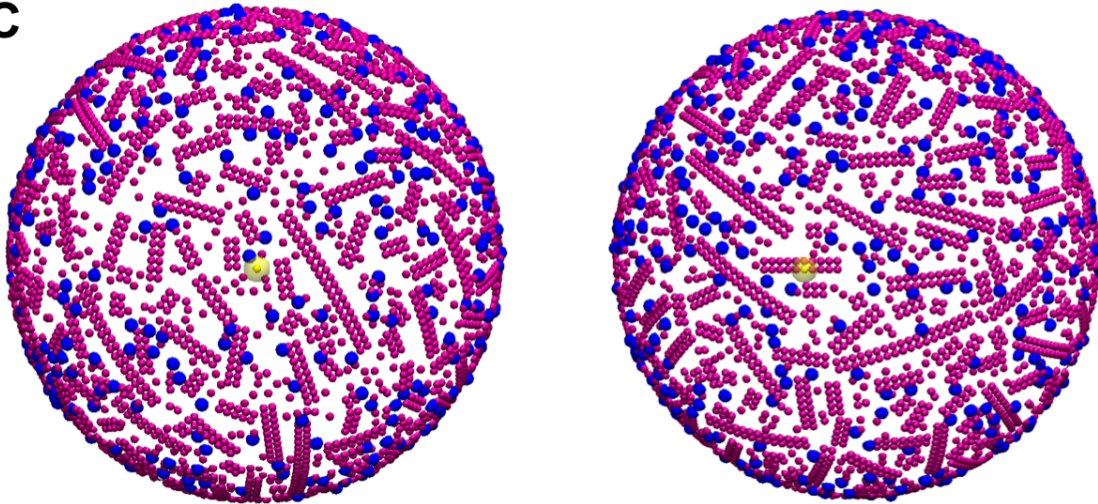
FIGURE S8: Derivation of rack size distribution by image analysis and resulting geometry (*A*) Microscopic image from Fotiadis et al., Nature 2003. Adapted by permission from Macmillan Publishers Ltd: Fotiadis et al, Nature. 421: 127–128, copyright 2003. (22), overlayed with markers for racks that could be identified individually (*green*). (*B*) Histogram of the rack size distribution in A, based on the identified racks. (*C*) Resulting geometries from the rack distribution on a disk vesicle with parameters as given in Table 1. R* is depicted once as monomeric (*left*) and once as part of a rack (*right*). Note, that the density in our models is 25,000 R μm^{-2}, as opposed to 50,000 R μm^{-2} in (22).

Supporting References

1.   Segel, I.H. 1975. Enzyme Kinetics. John Wiley & Sons, Inc.

2.   Heck, M., and K.P. Hofmann. 2001. Maximal rate and nucleotide dependence of rhodopsin-catalyzed transducin activation - Initial rate analysis based on a double displacement mechanism. Journal of Biological Chemistry. 276: 10000–10009.

3.   Kühn, H., N. Bennett, M. Michel-Villaz, and M. Chabre. 1981. Interactions between photoexcited rhodopsin and GTP-binding protein: kinetic and stoichiometric analyses from light-scattering changes. Proc. Natl. Acad. Sci. USA. 78: 6873–6877.

4.   Heck, M., A. Pulvermüller, and K.P. Hofmann. 2000. Light scattering methods to monitor interactions between rhodopsin-containing membranes and soluble proteins. Meth. Enzymol. 315: 329–347.

5.   Parkes, J.H., and P.A. Liebman. 1984. Temperature and pH dependence of the metarhodopsin I-metarhodopsin II kinetics and equilibria in bovine rod disk membrane suspensions. Biochemistry. 23: 5054–5061.

6.   Jäger, S., I. Szundi, J.W. Lewis, T.L. Mah, and D.S. Kliger. 1998. Effects of pH on rhodopsin photointermediates from lumirhodopsin to metarhodopsin II. Biochemistry. 37: 6998–7005.

7.   Okada, T., M. Sugihara, A.-N. Bondar, M. Elstner, P. Entel, et al. 2004. The Retinal Conformation and its Environment in Rhodopsin in Light of a New 2.2Å Crystal Structure. J.Mol.Biol. 342: 571–583.

8.   Choe, H.-W., Y.J. Kim, J.H. Park, T. Morizumi, E.F. Pai, et al. 2012. Crystal structure of metarhodopsin II. Nature. 471: 651–655.

9.   Lambright, D.G., J. Sondek, A. Bohm, N.P. Skiba, H.E. Hamm, et al. 1996. The 2.0 A crystal structure of a heterotrimeric G protein. Nature. 379: 311–320.

10.   Rasmussen, S.G.F., B.T. DeVree, Y. Zou, A.C. Kruse, K.Y. Chung, et al. 2012. Crystal structure of the b. Nature. 477: 549–555.

11.   Seitz, H.R., M. Heck, K.P. Hofmann, T. Alt, J. Pellaud, et al. 1999. Molecular Determinants of the Reversible Membrane Anchorage of the G-Protein Transducin. Biochemistry. 38: 7950–7960.

12.   Schöneberg, J., and F. Noé. 2013. ReaDDy - A Software for Particle-Based Reaction-Diffusion Dynamics in Crowded Cellular Environments. PloS One. 8: e74261.

13.   Kung, C., and J. Reed. 1986. Microviscosity Measurements of Phospholipid Bilayers Using Fluorescent Dyes That Undergo Torsional Relaxation. Biochemistry. 25: 6114–6121.

14.   Liebman, P., and G. Entine. 1974. Lateral Diffusion of Visual Pigment in Photoreceptor Disk Membranes. Science. 185: 457–459.

15.   Takezoe, H., and H. Yu. 1981. Lateral diffusion of photopigments in photoreceptor disk membrane vesicles by the dynamic Kerr effect. Biochemistry. 20: 5275–5281.

16.   Gupta, B., and T. Williams. 1990. Lateral diffusion of visual pigments in toad (Bufo marinus) rods and in catfish (Ictalurus punctatus) cones. The Journal of Physiology.

17.   Wang, Q., X. Zhang, L. Zhang, F. He, G. Zhang, et al. 2008. Activation-dependent Hindrance of Photoreceptor G Protein Diffusion by Lipid Microdomains. Journal of Biological Chemistry. 283: 30015–30024.

18.   Govardovskii, V., D. Korenyak, S. Shukolyukov, and L. Zueva. 2009. Lateral diffusion of rhodopsin in photoreceptor membrane: a reappraisal. Molecular Vision. 15: 1717–1729.

19.   Najafi, M., M. Haeri, B. Knock, W. Schiesser, and P. Calvert. 2012. Impact of signaling microcompartment geometry on GPCR dynamics in live retinal photoreceptors. Current Biology. 23: 1–18.

20.   Pugh, E., and T. Lamb. 1993. Amplification and kinetics of the activation steps in phototransduction. Biochim Biophys Acta. 1141: 111–149.

21.   Erban, R., and S.J. Chapman. 2009. Stochastic modelling of reaction-diffusion processes: algorithms for bimolecular reactions. Physical biology. 6: 046001.

22.   Fotiadis, D., Y. Liang, S. Filipek, D. Saperstein, A. Engel, et al. 2003. Atomic-force microscopyRhodopsin dimers in native disc membranes. Nature. 421: 127–128.